Title
Visualizing voltage activation with single particle cryoEM

Author
Dickinson, Miles Sasha

Publication Date
2020

Peer reviewed|Thesis/dissertation

Visualizing voltage activation with single particle cryoEM

by
Sasha Dickinson

DISSERTATION
Submitted in partial satisfaction of the requirements for degree of
DOCTOR OF PHILOSOPHY

in

Chemistry and Chemical Biology

in the

GRADUATE DIVISION
of the
UNIVERSITY OF CALIFORNIA, SAN FRANCISCO

Approved:

DocuSigned by:
Robert Stroud
CBB5A776502F413...

Robert Stroud
Chair

DocuSigned by:
David Agard

David Agard

DocuSigned by:
Michael Grabe
5B8B990D587B414...

Michael Grabe

Committee Members

Acknowledgments

I have too many people to be grateful to in far too many ways, so I will keep my acknowledgements brief. Firstly I would like to acknowledge my thesis advisor Bob Stroud who has been an exceptionally supportive presence throughout my time at UCSF. My colleagues from within the Stroud lab have also maintained a superlative environment for science and creativity, and I am very thankful to them for their kindness and for welcoming me. I also acknowledge my thesis committee consisting of David Agard and Michael Grabe, who have guided me along my scientific journey and have engaged with me in extremely productive discourse about my projects. I would like to specifically thank my collaborators, namely Alexander Myasnikov, Nicole Poweleit, Jacob Eriksen, Jinping Lu, Irene Marten, Rainer Hedrich, Kate Kim, and Meghna Gupta, from each of whom I have learned and benefited immensely. Finally I would like to acknowledge my family and friends, without whom I would not have accomplished anything.

Contributions

Chapter 1 of this manuscript is adapted from the following publication:

Resting state structure of the hyperdepolarization activated two-pore channel 3
Miles Sasha Dickinson, Alexander Myasnikov, Jacob Eriksen, Nicole Poweleit, Robert M. Stroud. Proceedings of the National Academy of Sciences Jan 2020, 117 (4) 1988-1993; DOI: 10.1073/pnas.1915144117

Chapter 2 is recently submitted work, done in collaboration with Jinping Lu, Irene Marten and Rainer Hedrich of the University of Würzburg, Germany.

Projects done in collaboration with Kate Kim and Meghna Gupta are not described here, but I acknowledge their immense role in shaping the course of my PhD.

Abstract

Visualizing voltage activation with single particle cryoEM

Miles Sasha Dickinson

Voltage-gated ion channels (VGICs) use voltage sensing domains (VSD) to sense the change in electrical potential across biological membranes and alter the open probability of a central channel. VSDs are composed of a four helix bundle in which one helix carries charged residues that move in response to changes in transmembrane electric field. Voltage sensors usually adopt a 'resting state' when the membrane is at 'resting potential', approximately -80 mV for most plasma membranes. As the membrane potential vanishes during depolarization - such as during the first phase of an action potential - so does the downwards force on the cationic side chains causing them to move across the membrane. This conformational change is conveyed to the central pore, which dilates to allow the diffusion of ions down their electrochemical gradients. The exact nature of this conformational change has been the subject of decades of biophysical investigation, though to this date only a few structural examples exist of voltage sensors in multiple conformations. Using a combination of single particle cryogenic electron microscopy (cryoEM) and electrophysiology, I have determined how a family of intracellular VGICs - two-pore channels (TPCs) - respond to changes in membrane potential providing new insights into the biophysics of voltage activation.

Table of Contents

List of Figures

List of Tables

Chapter 1

Resting state structure of the hyper-depolarization activated two-pore channel 3

Abstract

Voltage-gated ion channels endow membranes with excitability and the means to propagate action potentials that form the basis of all neuronal signaling. We determined the structure of a voltage-gated sodium channel, two-pore channel 3 (TPC3), which generates ultra-long action potentials. TPC3 is distinguished by activation only at extreme membrane depolarization ($V_{50} \approx +75$ mV), in contrast to other TPCs and Na_V channels that activate between -20 and 0 mV. We present electrophysiological evidence that TPC3 voltage activation depends only on voltage sensing domain 2 (VSD2), and that each of the three gating arginines in VSD2 reduces the activation threshold. The structure presents a chemical basis for sodium selectivity, and a constricted gate suggests a closed pore consistent with extreme voltage dependence. The structure, confirmed by our electrophysiology, illustrates the configuration of a bona-fide resting state voltage sensor, observed without the need for any inhibitory ligand, and independent of any chemical, or mutagenic alteration.

Main Text

Voltage-gated ion channels (VGICs) use changes in electrical potential across biological membranes to modulate their open probability (1, 2). These channels use a voltage sensing domain (VSD) containing basic residues to couple changes in trans-membrane voltage to dilation of a central pore domain through which ions diffuse (3, 4). Excitable membranes contain VGICs which usually activate upon membrane

depolarization and most exhibit maximal highest open probability at ~ 0 mV (5). While many groups have studied voltage activation using a variety of biophysical techniques (1, 6-10), resting conformations have eluded structural characterization (1, 2). VSD activation is typically described as charge translocation across a charge transfer center (CTC), whereby positively charged arginine side chains in the resting-state move away from an intracellular negative cluster (INC), across an insulating hydrophobic constriction site (HCS), to form interactions with an extracellular negative cluster (ENC). Recent structures from the two-pore channel family (11, 12), and of toxin-bound $Na_V1.7$ channels (13, 14) provided the first glimpses of 'resting' state VSDs by virtue of VSD-binding ions or ligands that inhibit voltage activation until above 0 mV, the condition in a crystal lattice or single particle EM experiment.

The two-pore channel family comprises three cation channels (TPC1-3), each dimers of tandem *Shaker*-like domains, that then dimerize to form a single functional channel. TPC1/3 are voltage-gated by virtue of positively charged arginine-containing voltage sensing domains, whereas TPC2 is lipid-gated (15, 16). TPCs were first identified in *Arabidopsis thaliana*, where a slow-activating, depolarization-elicited current in the vacuole was detected (17). The channel responsible was TPC1, which in plants forms a non-selective voltage-gated cation channel in the vacuolar membrane that undergoes diverse regulation by Ca^{2+}, lipids and phosphorylation (12, 16). Vertebrate and mammalian TPCs are Na^+ selective channels primarily localized to endolysosomal membranes (18, 19), and their activity is tuned by PIP_2 and association with, or phosphorylation by, mTORC1 (20). Despite encompassing only three members, the

TPC family exhibits remarkable functional diversity, and the physiological roles of these channels are still largely unknown (16, 21, 22).

Cang and colleagues (23) provided the first characterization of the molecular properties of TPC3, which they determined is plasma membrane-localized, Na^+ selective, and activated only at very large depolarization (e.g. $V_{50} \approx +75$ mV). Owing to functional similarity, they established that TPC3 forms the endogenous voltage-gated Na^+ channel on the plasma membrane of *Xenopus laevis* oocytes. Mammalian TPC3, however, is primarily localized to endolysosomal membranes and contributes to the regulation of membrane sorting, suggesting that the role of TPC3 may vary significantly across species (24). TPC3 does not inactivate and is probably responsible for generating or maintaining ultra-long action potentials, the phenomenon of prolonged membrane depolarization (23). Such processes appear to be widespread in the eggs of many species, including during fertilization-induced excitation in *Xenopus* (25) and Ca^{2+}-activated currents that last multiple minutes in worms (26, 27). Similar phenomena are also observed in TPC1 which generates ultra-long action potentials in plant vacuoles (28).

By virtue of the unique, hyper-depolarized activation of TPC3, we hypothesized that we could structurally capture TPC3 in a VSD resting conformation (fig. 1e). Unlike AtTPC1, whose resting state was determined by, and crystallographically accessed by occupation of an external Ca^{2+} binding site (11, 12) that positively shifts the activation potential, TPC3 does not require ions or small molecules to attenuate its voltage

sensitivity, suggesting that the channel contains an intrinsic mechanism to suppress activation. Therefore, we turned to TPC3 as a first example of a stable resting state VGIC channel. We purified glycodiosgenin-solubilized TPC3 from HEK293F cells and used electron cryo-microscopy to determine a structure to 3.2 Å resolution (fig. 1a), that enabed complete and unambiguous placement of residues and side chains in all transmembrane helices. In conjunction with voltage clamp electrophysiology, we defined the role of the VSDs in voltage activation and provide a snapshot of a first definitively resting state VSD that does not depend on any ion, toxin or ligand.

TPC3 is a C2 symmetric channel with 'domain-permuted' voltage sensing and pore domains, in which the VSD1 interacts with the pore domain 2 around the pore structures (fig. 1b-d). Domains I and II of TPC3 contain homologous voltage sensing domains, each comprised of three arginine residues in the fourth TM helix: R166, R169 and R172 in S4 (corresponding to R2-R4 of the Shaker K^+ channel) and R522, R525 and R528 in S10 (corresponding to R3-R5 of Shaker).

By electrophysiology we show that only one voltage sensor, VSD2, is responsible for voltage activation, and that R3, R4, and R5 within S10 in it each sensitize the channel to voltage. To interrogate the role of each VSD arginine in voltage sensing, we neutralized each one in turn and recorded currents from cells expressing mutants. VSD1 has no effect: R166Q and R169Q (R3 and R4 of VSD1) have no effect on voltage dependence relative to wild type (fig. 2e). We had difficulty recording from R172Q (R5 of VSD1) because of intracellular retention, probably due to misfolding of the protein,

however in rare cases we did observe wild type-like currents. R522Q, R525Q and R528Q in VSD2 each shift the voltage dependence further toward the positive (fig. 2d-e), indicating that all three S10 arginines cooperate in activation. Triple mutants (R to Q) on either of the VSDs (denoted ΔVSD1/2) confirmed that VSD2 alone controls voltage gating. These data contrast with mammalian TPC1 where analogous mutations in VSD2 either inhibit or constitutively activate the channel, whereas in TPC3 they mimic the plant TPC1 phenotype where all R to Q mutations inhibit voltage activation (11, 21, 29).

In the inactive VSD1, S4 adopts an α-helical fold near the S4-S5 linker, but lacks secondary structure at the S3-S4 loop. The arginines in S4 are clearly accessible to extracellular solvent and make strong coulombic and salt-bridge interactions with the extracellular negative cluster (ENC). R169 forms a strong interaction with E566 of S11, non-covalently stapling S4 to the pore domain. The arrangement of both the basic and acidic residues aligns very well with that of VSD1 in mTPC1 and both lack the common features of a voltage sensing helix, congruent with voltage independence (fig. 2a).

In the active VSD2, S10 of TPC3 contains three arginines, unlike mammalian TPC1 that has only two. Y455 forms the hydrophobic constriction site (HCS) of the charge transfer center (CTC). R4 and R5 are situated below Y455 with R4 forming a cation-π interaction with the phenol ring (fig. 2a). The most extracellular arginine, R3 points upwards but is slightly displaced from interaction with the extracellular negative cluster. This is in contrast to the active state VSDs of Na_VAb (30) and Na_VRh (31)in which R3 faces outward and is in contact with the ENC while R1, R2 even more toward

the extracellular side, point toward the outside surface (an active state VSD conformation). S10 adopts a 3_{10}-helical fold as is observed in other S4 helices, such that the arginines stack into the interior of the four-helix bundle (fig. 2a). Three basic residues, K219, K223 and R224, on the extracellular extreme of the pore helix S11 are in proximity with the extracellular negative cluster (ENC), although the weak density for such residues precludes accurate determination of the side chains. Such basic residues are not present in TPC1, and the hypothetical interaction is located where the inhibitory Ca^{2+} acts in plant TPC1(32). Hence, such interactions may either exclude the S10 arginines from forming their active state interactions with the ENC or potentially couple the electrical state of VSD2 to the pore domain.

While VSD2 of mTPC1 and TPC3 align well with each other as rigid bodies in isolation, alignment of the two channels based on the pore domain shows that the two domains are out of register (fig. 2e). Alignment of the two channels based on one VSD2 bundle shows high similarity in VSD2 (~ 0.9 Å rmsd) and large differences in the rest of the channel (~ 5.5 Å rmsd), including in the other VSD2 (fig. 2f). If mTPC1 and TPC3 share common activation processes, this may represent an early conformation during activation, prior to the electromechanical coupling step of pore opening. Activation of VSD2 may, hence, involve a combination of rigid body motion of the entire four helix bundle relative to the pore, and the upwards translocation of R3 towards the ENC and R4 across the HCS. The potential aforementioned interactions between the VSD2 ENC and the S11 basic residues may hinder such a conformation rearrangement, helping to explain the large energetic barrier to voltage activation.

The channel pore is tightly closed, consistent with a non-conducting state (fig. 3a-b). The selectivity filter, formed by filter 1 and filter 2 of domains 1 and 2, respectively, is defined by a coin slot entry suitable for partially hydrated Na^+ ions, similar to that observed in recent sodium-selective TPC structures. Filter 2 is formed by orthogonal Q625 and N624 pairs with distances of 5.6 and 4.3 Å respectively, likely conferring Na^+ selectivity. Below the asparagine pair is filter 1 consisting of the amide carbonyl of A252 and the amide carbonyl of T251 with pairwise distances of 7.1 and 6.2 Å, respectively. A putative sodium ion (the only monoatomic cation in solution) is situated between the carbonyl oxygen and sidechain hydroxyl of T251. Below the filter is an aqueous cavity lined by small hydrophobic side chains. Beneath the cavity is the gate, formed by constriction points at L288 (3.79 Å), L665 (4.02 Å) and Y292 (5.58 Å), too narrow to allow the passage of hydrated ions (fig. 3b-d).

We observe multiple well-ordered lipids tightly associated with the channel (fig. 4a). One upper leaflet lipid is located in the same site that inhibitor NED-19 occupies in the *Arabidopsis* TPC1 crystal structure. We observe a lipid-like density at the S4-S5 linker (i.e. lower leaflet), similar in location to the PIP_2 regulatory site in mTPC1. The lipid, with a small head-group poised towards the membrane, looks distinct from the phosphatidylcholine-like upper leaflet lipids, and resembles a phosphatidic acid. This would be consistent with the observed lower leaflet phosphatidic acid at the S10-S11 linker in AtTPC1, and the proposed functional role of phosphatidic acids in TPC physiology (12, 16). No lipids were supplemented during purification so all observed

density belongs to co-purified species. We confirmed the observation of Cang et al. that TPC3 is insensitive to $PI(3,5)P_2$ and $PI(4,5)P_2$ administered through the pipette solution during whole cell voltage clamp recordings (33), and we additionally determined that $PI(3,4)P_2$ has no apparent effect at concentrations up to 100 μM.

The structure of TPC3 should represent a profoundly resting state VSD configuration as demonstrated by electrophysiology. Since most structures of VGICs represent a VSD-activated state, this, and the structural rearrangements observed during AtTPC1 voltage activation (34) suggest that the mechanisms of voltage activation in TPCs may involve more complex conformational changes than the classical models of voltage sensors would predict. Substantial motions in the VSD, driven by positive membrane potential, may be necessary to open the activation gate. These may include in-plane motions of the VSD which can be sensed either through the S10-S11 linker or the extracellular salt bridges, or the non-covalent interactions between S10 and the pore domain. Understanding the exact nature of these conformational changes and how they couple to gating charge translocation will provide fundamental insights into how ‘modular’ voltage sensing domains can exhibit exquisite functional diversity.

Acknowledgments

We thank Alexander Kintzer for help with construct design and screening; Phuong Nguyen and Alisa Bowen for assistance with mammalian cell culture; Axel Brilot for data processing advice; Michael Braunfeld and David Bulkley for maintenance of the

UCSF EM facility and the NIH for their support of our facility. We also thank Janet Finer-Moore, Sergei Pourmal and Evan Green for critical reading of the manuscript. **Funding:** The research was funded by NIH grant R01 GM24485 (to R.M.S.). M.S.D. acknowledges an NSF graduate research fellowship. **Author contributions:** M.S.D. conceived of the project and designed all experiments under the supervision of R.M.S. A.M. and N.P. assisted with microscopy data acquisition. J.E. and M.S.D. collected electrophysiology data. M.S.D. and R.M.S. wrote the manuscript. R.M.S. obtained funding for this research. **Competing interests:** Authors declare no competing interests. **Data and materials availability:** The sharpened and unsharpened maps are available in the EMDB (accession no. 21015); and the model has been deposited into the PDB (accession no. 6V1Q). The DrTPC3, wild type and mutant, pEG_BacMam plasmids are available upon request.

Methods

Protein expression and purification

Orthologs of TPC3 were screened for expression and biochemical behavior using fluorescence size exclusion chromatography (FSEC) (35). HEK 293T cells were transfected with eGFP fusions of orthologs in a pEG_Bacmam vector using JetPrime transfection reagent. 48 hr. post transfection, cells were washed with ice cold PBS and solubilized in 20 mM Tris pH 7.4, 150 mM NaCl, 1 mM PMSF and 1% β-dodecyl maltoside, overnight. The suspension was centrifuged at 40,000 rpm (TLA-55 rotor) for 1 hr. before injection over a Superose 6 gel filtration column in line with a fluorescence detector (ex/em = 488nm/510nm). Additive and detergent screens were performed in a

similar manner to determine optimal buffer conditions for purification. TPC3 from *Danio rerio* (DrTPC3) was expressed as a C-terminal eGFP fusion in a pEG plasmid using the Bacmam system in HEK GnTi^{-} cells. Cells were harvested 48 hr. post induction with 10 mM sodium butyrate. The cell pellets were resuspended in buffer A (20 mM Tris pH 7.4, 150 mM NaCl) and stored at -80°C until use. All subsequent steps were performed at 4^{o}C. Cells were thawed, PMSF was added to 1 mM and Roche cOmplete protease inhibitor cocktail was added at 1 tablet per 100 mL. Cells were lysed by sonication on ice at 1 s^{-1} for 5 minutes. Glycodiosgenin was added to the lysate to a final concentration of 1%. After 8 hr. of solubilization, the lysate was centrifuged at 30,000 rpm for 40 minutes (Ti45 rotor) to remove insoluble material. The clarified lysate was filtered through a 0.22 um filter and batch bound to anti-GFP nanobody-conjugated sepharose (made in house) for 2 hr. with gentle nutation. The flow through was collected and the resin was washed with 20 column volumes of buffer B (20 mM Tris pH 7.4, 150 mM NaCl, 0.06% glycodiosgenin). The washed resin was resuspended in buffer B with 2 mM $CaCl_2$ and 200 U thrombin for on-column cleavage overnight. The eluate was collected and concentrated before injection over a Superose 6 gel filtration column. Peak fractions were pooled and concentrated to ~ 3 mg mL^{-1} for vitrification. Grids for electron cryo-microscopy were prepared using a Mark IV Vitrobot, in which 4.5 µL of sample was applied to freshly glow discharged Quantifoil Cu R1.2/1.3 holey carbon grids, blotted for 4 seconds at 100% humidity and plunge frozen in liquid N_2-cooled ethane. Grids were screened for ice quality on a Talos Arctica microscope before extensive data collection.

Microscopy

Movies were acquired on a 300 keV Titan Krios equipped with a Gatan Imaging Filter (20 eV slit width) and K2 Summit camera (operating in super-resolution mode). The pixel size on the specimen was 0.407 Å pix^{-1}. Movies were collected with 100 frames over 10 s (0.1 s dose fractionation), using a per frame dose of 0.92 e^{-} $Å^{-2}$ (92 e^{-} $Å^{-2}$ accumulated dose), over an underfocus range of 0.8 to 2.0 µm. Movies were drift corrected and dose weighted with MotionCor2 (36) using 5 by 5 patches and twice Fourier binned to a pixel size of 0.814 Å pix^{-1}. SerialEM (Mastronarde) and Focus (37) were used for data acquisition and on-the-fly drift correction, respectively.

Image processing

CTF estimation was performed using CTFFIND4 and 1,201,080 particles were picked *ab initio* from 7118 micrographs using cisTEM (38). The particles were subjected to 2D classification in cisTEM, from which 706,801 particles were selected. These particles were used to calculate a 3D *ab initio* template in cisTEM. The coordinates were exported to Relion 3.0 (39) and particles were extracted twice binned, resulting in a box size of 216 pix and a pixel size of 1.628 Å pix^{-1}. Unmasked 3D classification into 6 classes was performed in Relion 3.0 using the twice down-sampled *ab initio* map as reference, low-pass filtered to 60 Å. Two classes constituting 213,328 particles were selected and subjected to 3D auto-refine in Relion 3.0 resulting in a 3.75 Å reconstruction. This map was used to calculate a micelle-excluding mask for use in a 'skip-align' 3D classification into 8 classes in Relion 3.0. Two classes representing 170,446 particles were selected. The particles were re-extracted in Relion un-binned

and exported to cisTEM using ‘relion stack create’ and refined while applying the aforementioned mask (down-weighting and filtering the exterior to 0.1 and 30 Å, respectively), excluding frequencies past 7 Å during alignment. Multiple rounds of masked refinement in cisTEM resulted in a 3.2 Å reconstruction according to Fourier shell correlation using a 0.143 cutoff. Simultaneously, the Relion particle stack was subjected to non-uniform refinement in cryoSPARC v2 (40), resulting in a 3.1 Å reconstruction. The cisTEM and cryoSPARC maps are of similar quality and nominal global resolution and both were used for model building.

Model building

The TPC3 atomic model was built *de novo* using a MODELLER-generated homology model (41) as a guide. All model building was performed in Coot (42). The final model was refined using phenix_real_space_refine (43). Map and model figures were prepared using UCSF Chimera (44). Residues 320-407, corresponding to the cytosolic linker between domains 1 and 2, were not modeled due to poor resolution.

Electrophysiology

Voltage clamp recording of DrTPC3 and mutants was performed in whole cell configuration using a Axoclamp 200B amplifier and a Digidata 1440A controlled by pClamp (Molecular Device). HEK293T cells were transiently transfected with DrTPC3-eGFP variants using the JetPrime transfection reagent. 48 hr. post transfection, the cells were trypsinized and plated at appropriate density on poly-L-lysine-coated coverslips. Cells with plasma membrane-localized GFP expression were selected for

recording. The pipette and bath solutions were adapted from Cang et al. (23) with symmetric [Na^+]. The bath solution consisted of 145 mM Na^+ methanesulphonate, 5 mM NaCl, 10 mM HEPES, 10 mM glucose pH 7.4. The pipette solution consisted of 130 mM Na-methanesulphonate, 2.5 mM MgCl2, 10 mM HEPES, 10 mM EGTA, 20 mM NaOH pH 7.2. Patch pipettes were pulled from borosilicate glass and flame polished to a resistance of 2-4 MOhm, and recordings were made from cells with an access resistance below 10 MOhm. Currents were acquired using a step protocol with 2s steps from -50 mV to +150 mV in 10 mV increments, from a holding potential of -70 mV. Data was analysed using Clampfit (Molecular device). Conductance was calculated using Ohm's law from steady state currents and fitted using a single Boltzmann sigmoid.

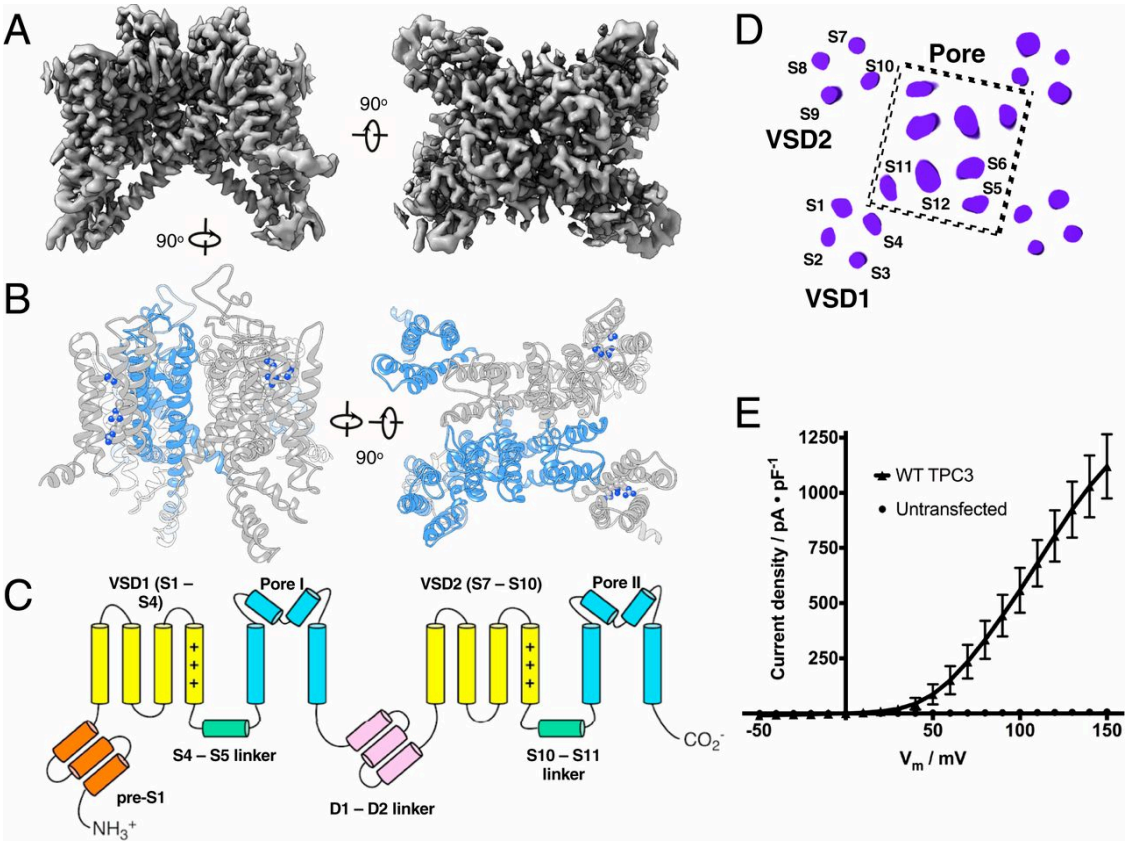

Fig. 1.1. Cryo-EM structure of two-pore channel 3. (A) Orthogonal views of the coulomb potential map of TPC3 sharpened with a B-factor of -90 Å^2. **(B)** Molecular model of TPC3 colored by subunit to illustrate domain swapping of pore and voltage sensor domains (right), and oriented to bring VSDs of the grey subunit to the front (left). VSD2 is on the left. Arginine sidechains of S4 and S10 are shown. **(C)** Annotated schematic of domain arrangement. **(D)** 2D arrangement of helices, viewed normal to a central slice through the channel. **(E)** Current density of wild type TPC3 showing its characteristic right-shifted response, determined by whole cell voltage clamp on HEK293T cells. All recordings use symmetric [Na^+] (n=6 cells).

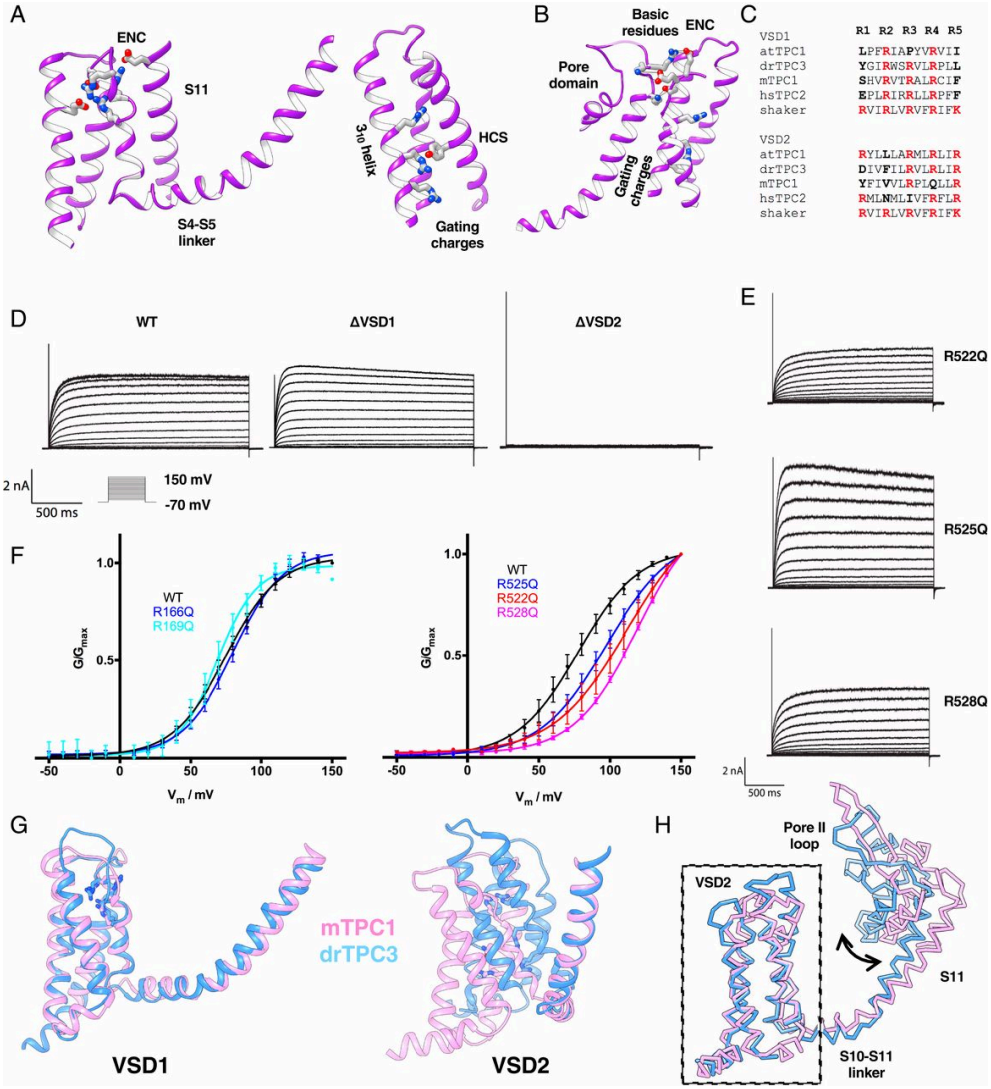

Fig. 1.2. Structural and functional asymmetry in the voltage sensing domains. (A) Structure of VSD1 showing the interactions of the arginines with the extracellular negative cluster (left). Structure of VSD2 showing interactions of R525 with the

hydrophobic constriction site Y455, and R528 with the intracellular solvent (right). **(B)** Implied interactions between basic residues on the S11 helix and the extracellular negative cluster in VSD2. **(C)** Sequence alignment of the S4 (top) and S10 helices (bottom) of zebrafish TPC3, *Arabidopsis* TPC1, mouse TPC1 and human TPC2 with respect to the Shaker K_V VSD. R1-R5 of the Shaker convention are in bold and basic residues are colored red. (**D**) Currents obtained from a voltage step protocol of wild type and arginine to glutamine triple mutants in VSD1 and VSD2. The VSD1 triple mutant resembles WT while the VSD2 triple mutant is silent. **(E)** Currents from the VSD2 R-Q point mutants. **(F)** Conductance curves of the channel with R-Q mutants in VSD1 (left) and VSD2 (right), calculated from their whole cell steady state currents using a voltage step protocol. The mean conductance of 6-8 cells each with standard deviation is shown and curves are fitted using a single Boltzmann sigmoid. **(G)** Conformational comparisons of VSD1 (left) and VSD2 (middle), of TPC3 (blue) and mTPC1 (PDB: 6C96) (pink), based on alignment of the S4-S5 linker and S5, or the S10-S11 linker and S11. (**H**) Comparison of the TPC3 versus mTPC1 pore domains based on alignment of their VSD2s to emphasize the differences between the two-domain conjugates in resting versus putatively activated/pre-activated states.

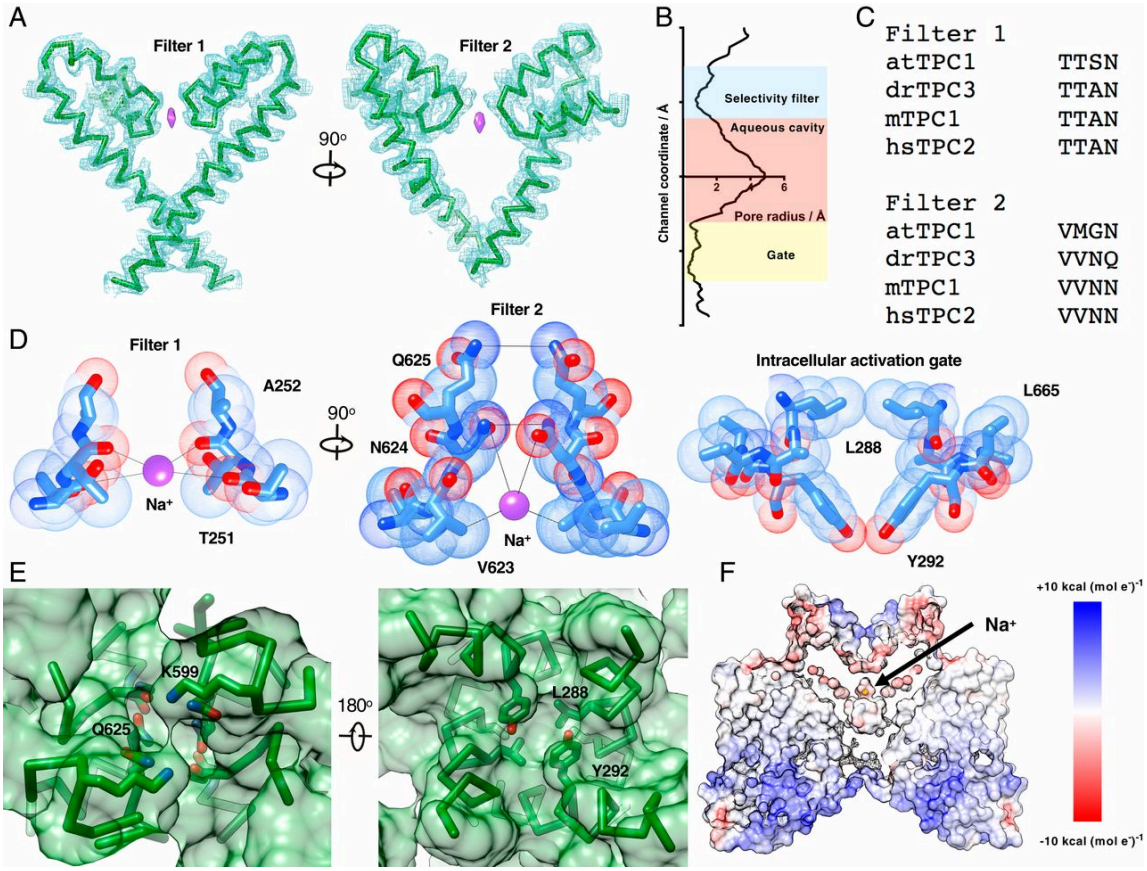

Fig. 1.3. Structural features of the ion conduction pathway. (A) Structure of the pore 1 (left) and pore 2 (right) with sharpened potential map. (**B)** Pore radius as a function of channel coordinate, roughly aligned to the molecule shown in figure 3a calculated using HOLE (45). **(C)** Sequence alignment of TPC selectivity filters. **(D)** Chemical features of the selectivity filter and gate with Van der Waals surface shown. **(E)** Surface representation illustrates a solvent-excluding selectivity filter (left) and intracellular activation gate (right). **(F)** Surface representation colored by Coulombic potential calculated in UCSF Chimera, illustrating the ion conduction pathway.

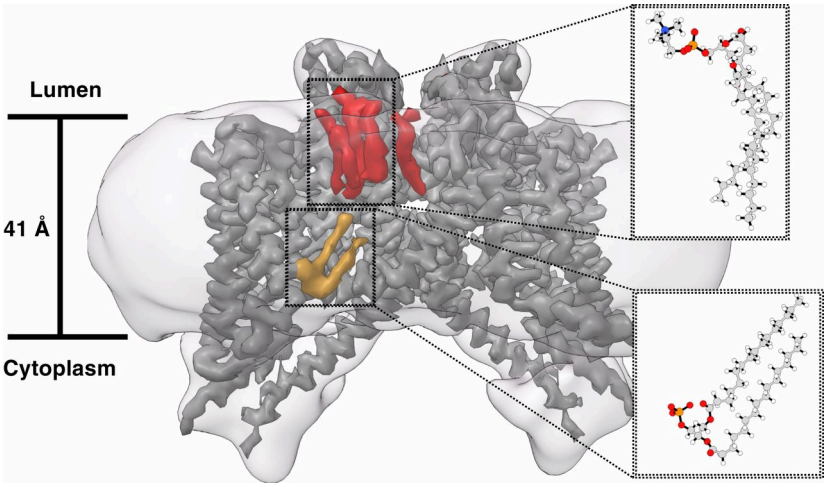

Fig. 1.4. Lipids interacting with the channel. (A) Sharpened potential map of TPC3 at high contour overlaid with lipidic densities at low contour colored orange (lower leaflet) and red (upper leaflet). The orange density resembles a phosphatidic acid, with generic chemical structure shown. The upper leaflet lipids have large head groups, similar to those in phosphatidylcholine-like lipids with generic chemical structure shown. The upper leaflet species on the right resembles a glycodiosgenin molecule given its single tail. The detergent micelle (low contour map) is shown to approximate the boundaries of the bilayer.

REFERENCES

1. B. Hille, Ion Channels of Excitable Membranes, 3rd Edition. Sinauer Associates, Sunderland, Mass. (2001).
2. W. A. Catterall, G. Wisedchaisri, N. Zheng, The chemical basis for electrical signaling. *Nat Chem Biol* **13**, 455-463 (2017).
3. F. Bezanilla, The voltage sensor in voltage-dependent ion channels. *Physiol Rev* **80**, 555-592 (2000).
4. F. Bezanilla, How membrane proteins sense voltage. *Nat Rev Mol Cell Biol* **9**, 323-332 (2008).
5. C. A. Ahern, J. Payandeh, F. Bosmans, B. Chanda, The hitchhiker's guide to the voltage-gated sodium channel galaxy. *J Gen Physiol* **147**, 1-24 (2016).
6. W. Stuhmer *et al.*, Structural parts involved in activation and inactivation of the sodium channel. *Nature* **339**, 597-603 (1989).
7. S. A. Seoh, D. Sigg, D. M. Papazian, F. Bezanilla, Voltage-sensing residues in the S2 and S4 segments of the Shaker K+ channel. *Neuron* **16**, 1159-1167 (1996).
8. C. S. Gandhi, E. Y. Isacoff, Molecular models of voltage sensing. *J Gen Physiol* **120**, 455-463 (2002).
9. C. A. Villalba-Galea, W. Sandtner, D. M. Starace, F. Bezanilla, S4-based voltage sensors have three major conformations. *Proc Natl Acad Sci U S A* **105**, 17600-17607 (2008).

10. X. Tao, A. Lee, W. Limapichat, D. A. Dougherty, R. MacKinnon, A gating charge transfer center in voltage sensors. *Science* **328**, 67-73 (2010).
11. J. Guo *et al.*, Structure of the voltage-gated two-pore channel TPC1 from Arabidopsis thaliana. *Nature* **531**, 196-201 (2016).
12. A. F. Kintzer, R. M. Stroud, Structure, inhibition and regulation of two-pore channel TPC1 from Arabidopsis thaliana. *Nature* **531**, 258-262 (2016).
13. T. Clairfeuille *et al.*, Structural basis of alpha-scorpion toxin action on Nav channels. *Science* **363** (2019).
14. H. Xu *et al.*, Structural Basis of Nav1.7 Inhibition by a Gating-Modifier Spider Toxin. *Cell* **176**, 702-715 e714 (2019).
15. P. J. Calcraft *et al.*, NAADP mobilizes calcium from acidic organelles through two-pore channels. *Nature* **459**, 596-600 (2009).
16. A. F. Kintzer, R. M. Stroud, On the structure and mechanism of two-pore channels. *FEBS J* **285**, 233-243 (2018).
17. R. Hedrich, E. Neher, Cytoplasmic Calcium Regulates Voltage-Dependent Ion Channels in Plant Vacuoles. *Nature* **329**, 833-836 (1987).
18. X. Wang *et al.*, TPC proteins are phosphoinositide- activated sodium-selective ion channels in endosomes and lysosomes. *Cell* **151**, 372-383 (2012).
19. H. Xu, D. Ren, Lysosomal physiology. *Annu Rev Physiol* **77**, 57-80 (2015).
20. C. Cang *et al.*, mTOR regulates lysosomal ATP-sensitive two-pore Na(+) channels to adapt to metabolic state. *Cell* **152**, 778-790 (2013).
21. J. She *et al.*, Structural insights into the voltage and phospholipid activation of the mammalian TPC1 channel. *Nature* **556**, 130-134 (2018).

22. J. She *et al.*, Structural mechanisms of phospholipid activation of the human TPC2 channel. *Elife* **8** (2019).

23. C. Cang, K. Aranda, D. Ren, A non-inactivating high-voltage-activated two-pore Na(+) channel that supports ultra-long action potentials and membrane bistability. *Nat Commun* **5**, 5015 (2014).

24. O. A. Ogunbayo *et al.*, Organelle-specific subunit interactions of the vertebrate two-pore channel family. *J Biol Chem* **290**, 1086-1095 (2015).

25. C. Baud, R. T. Kado, K. Marcher, Sodium channels induced by depolarization of the Xenopus laevis oocyte. *Proc Natl Acad Sci U S A* **79**, 3188-3192 (1982).

26. S. Miyazaki, K. Takahashi, K. Tsuda, Calcium and sodium contributions to regenerative responses in the embryonic excitable cell membrane. *Science* **176**, 1441-1443 (1972).

27. L. A. Jaffe, R. T. Kado, D. Kline, A calcium-activated sodium conductance produces a long-duration action potential in the egg of a nemertean worm. *J Physiol* **381**, 263-278 (1986).

28. D. Jaslan *et al.*, Voltage-dependent gating of SV channel TPC1 confers vacuole excitability. *Nat Commun* **10**, 2659 (2019).

29. D. Jaslan *et al.*, Gating of the two-pore cation channel AtTPC1 in the plant vacuole is based on a single voltage-sensing domain. *Plant Biol (Stuttg)* **18**, 750-760 (2016).

30. J. Payandeh, T. Scheuer, N. Zheng, W. A. Catterall, The crystal structure of a voltage-gated sodium channel. *Nature* **475**, 353-358 (2011).

31. X. Zhang *et al.*, Crystal structure of an orthologue of the NaChBac voltage-gated sodium channel. *Nature* **486**, 130-134 (2012).

32. B. Dadacz-Narloch *et al.*, A novel calcium binding site in the slow vacuolar cation channel TPC1 senses luminal calcium levels. *Plant Cell* **23**, 2696-2707 (2011).

33. C. L. Cang, B. Bekele, D. J. Ren, The voltage-gated sodium channel TPC1 confers endolysosomal excitability. *Nature Chemical Biology* **10**, 463-469 (2014).

34. A. F. Kintzer *et al.*, Structural basis for activation of voltage sensor domains in an ion channel TPC1. *Proc Natl Acad Sci U S A* **115**, E9095-E9104 (2018).

35. T. Kawate, E. Gouaux, Fluorescence-detection size-exclusion chromatography for precrystallization screening of integral membrane proteins. *Structure* **14**, 673-681 (2006).

36. S. Q. Zheng *et al.*, MotionCor2: anisotropic correction of beam-induced motion for improved cryo-electron microscopy. *Nat Methods* **14**, 331-332 (2017).

37. N. Biyani *et al.*, Focus: The interface between data collection and data processing in cryo-EM. *J Struct Biol* **198**, 124-133 (2017).

38. T. Grant, A. Rohou, N. Grigorieff, cisTEM, user-friendly software for single-particle image processing. *Elife* **7** (2018).

39. S. H. Scheres, RELION: implementation of a Bayesian approach to cryo-EM structure determination. *J Struct Biol* **180**, 519-530 (2012).

40. A. Punjani, J. L. Rubinstein, D. J. Fleet, M. A. Brubaker, cryoSPARC: algorithms for rapid unsupervised cryo-EM structure determination. *Nat Methods* **14**, 290-296 (2017).

41. A. Sali, T. L. Blundell, Comparative protein modelling by satisfaction of spatial restraints. *J Mol Biol* **234**, 779-815 (1993).

42. P. Emsley, B. Lohkamp, W. G. Scott, K. Cowtan, Features and development of Coot. *Acta Crystallogr D Biol Crystallogr* **66**, 486-501 (2010).

43. P. D. Adams *et al.*, PHENIX: a comprehensive Python-based system for macromolecular structure solution. *Acta Crystallogr D Biol Crystallogr* **66**, 213-221 (2010).

44. E. F. Pettersen *et al.*, UCSF Chimera--a visualization system for exploratory research and analysis. *J Comput Chem* **25**, 1605-1612 (2004).

45. O. S. Smart, J. G. Neduvelil, X. Wang, B. A. Wallace, M. S. Sansom, HOLE: a program for the analysis of the pore dimensions of ion channel structural models. *J Mol Graph* **14**, 354-360, 376 (1996).

Supplemental information for chapter 1

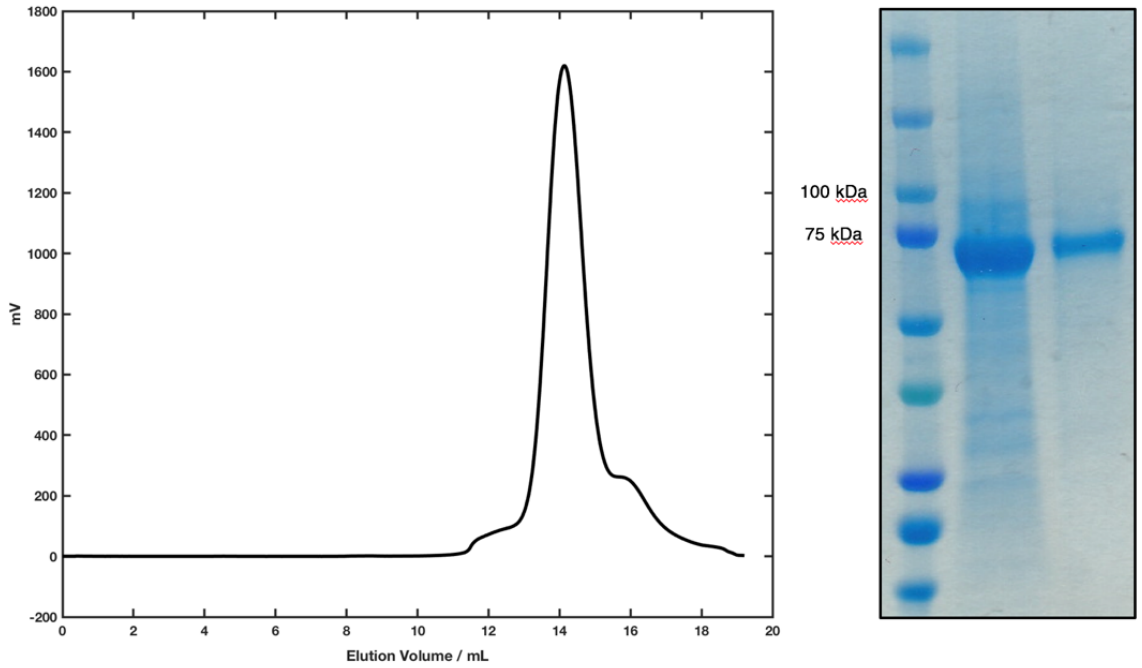

SFig. 1.1: Gel filtration chromatogram acquired using a Superose 6 increase 10/300 column. SDS-PAGE shows SEC input and peak fraction.

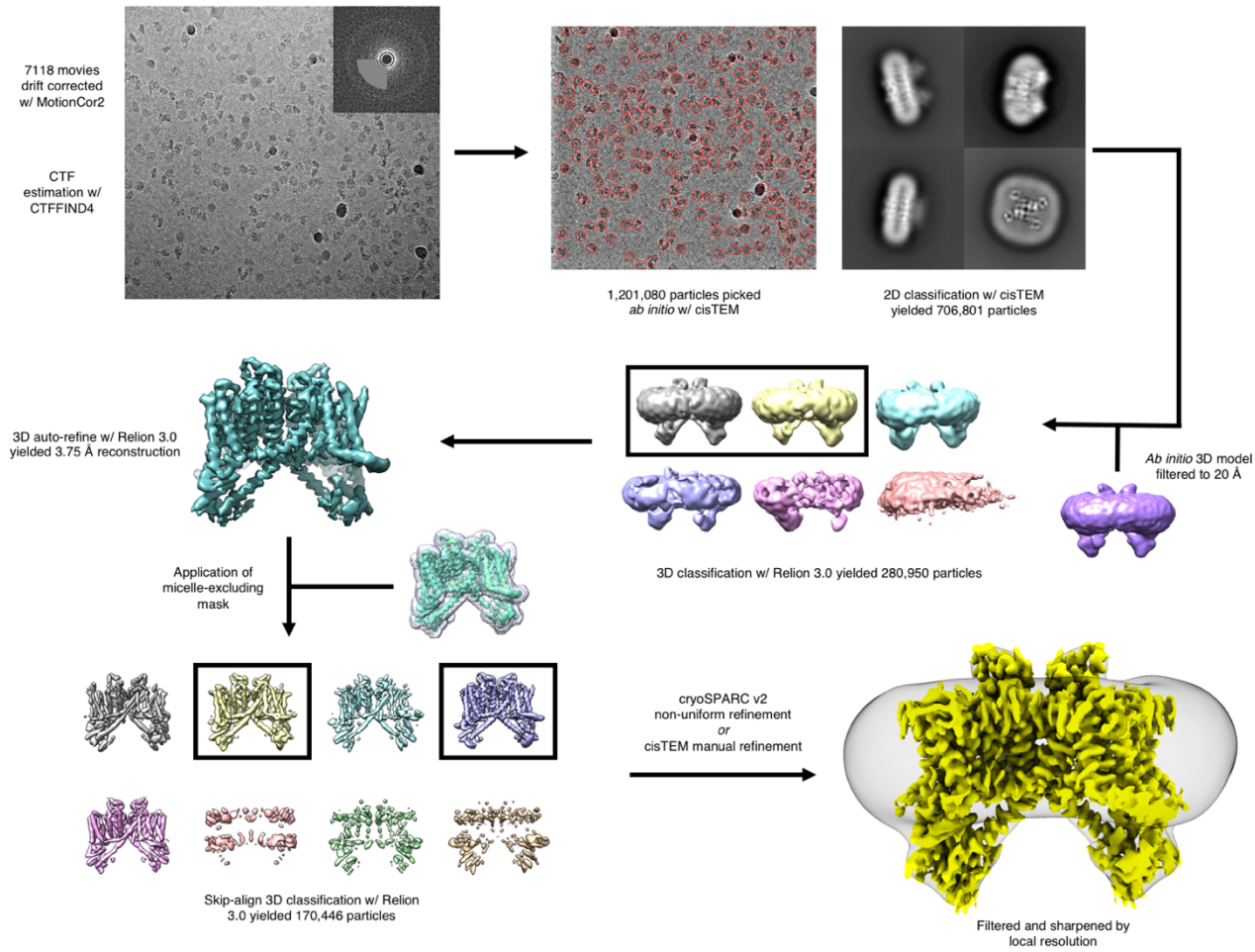

SFig. 1.2: Single particle pipeline for obtaining the TPC3 reconstruction.

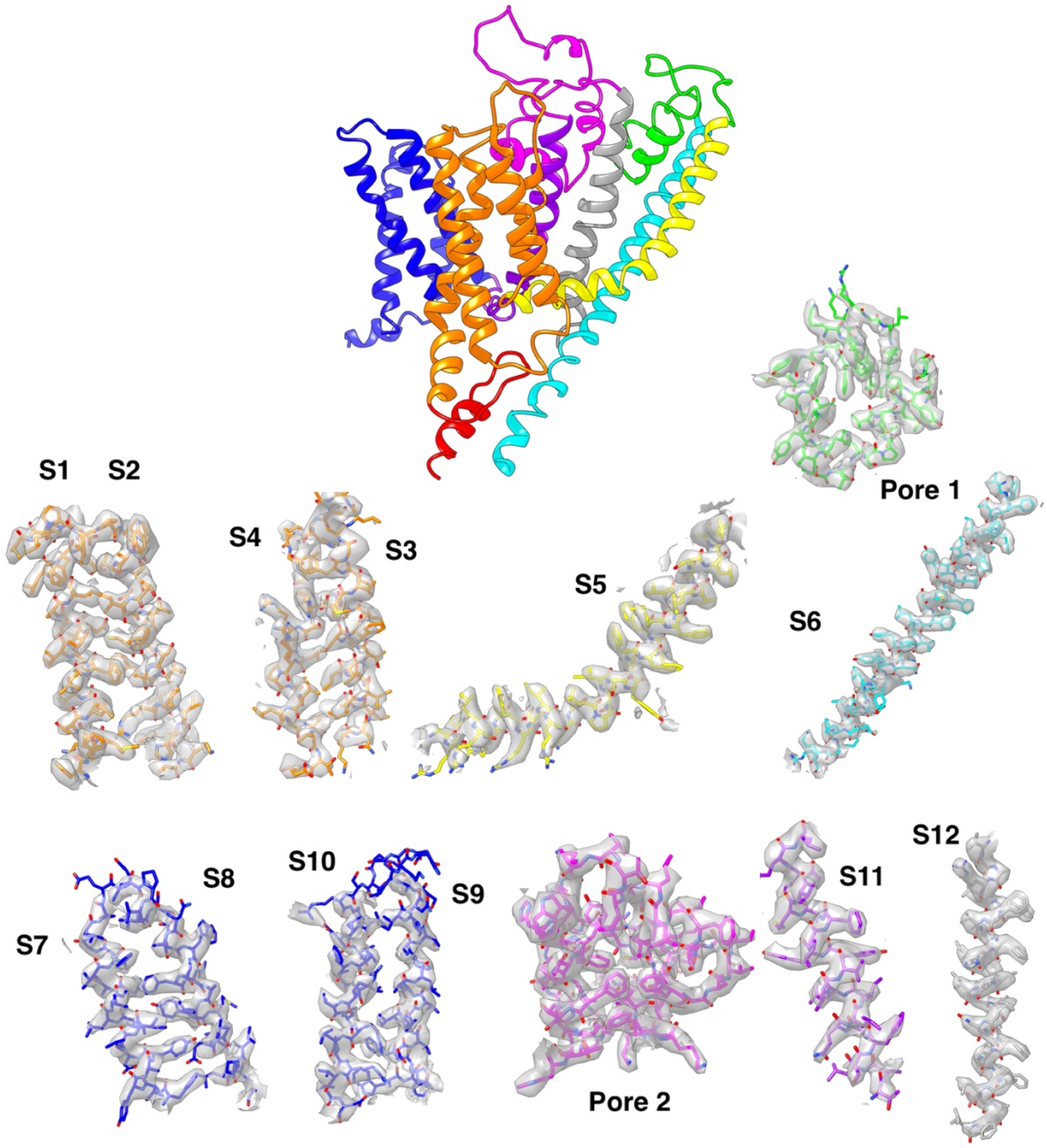

SFig. 1.3: Fit of the atomic model into the sharpened potential map.

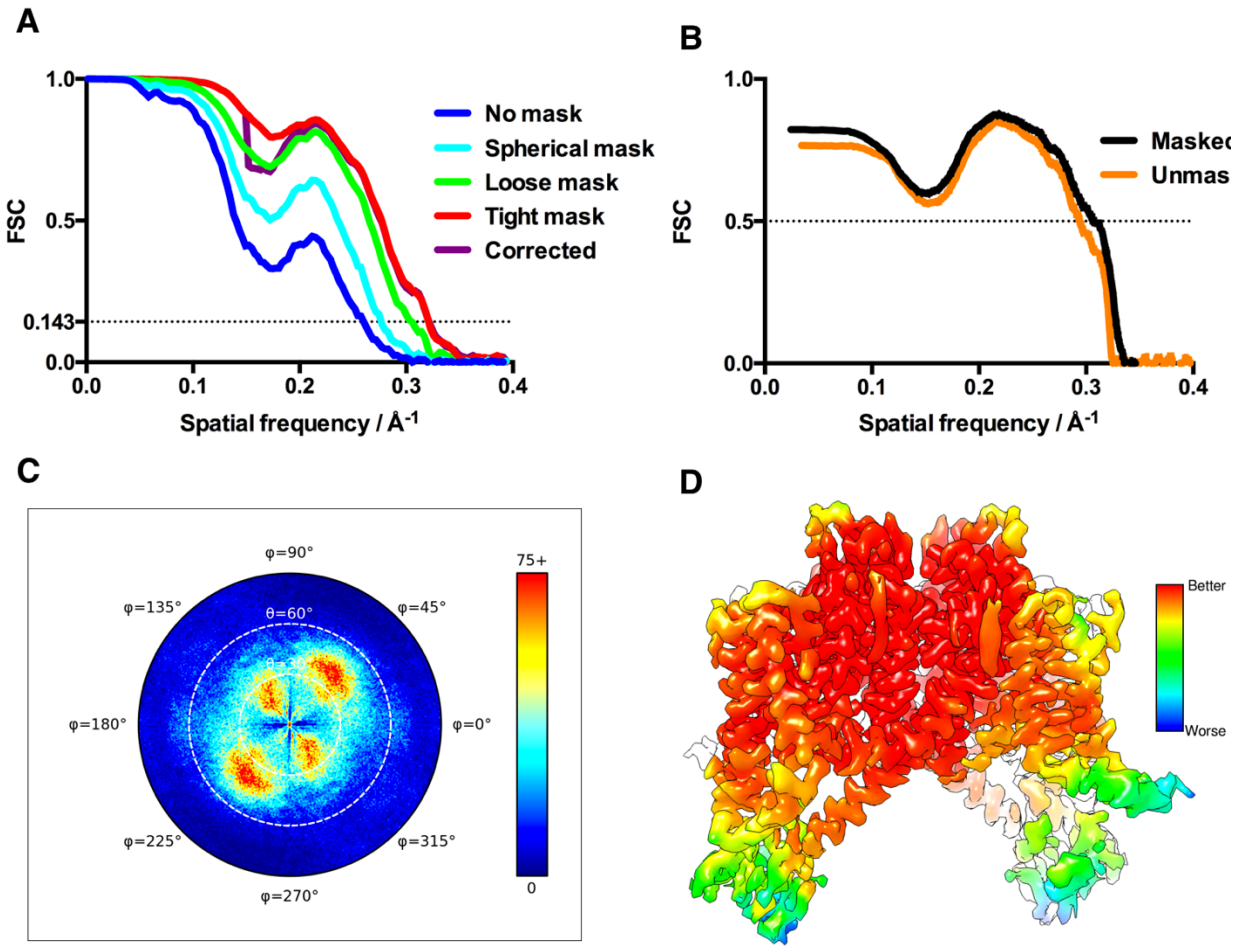

SFig. 1.4: (**A**) Fourier shell correlation of the cryoSPARC refinement, using a 0.143 threshold. (**B**) Map to model FSC using a 0.5 threshold. (**C**) Angular distribution plot of particles determined in cisTEM. (**D**) Final reconstruction colored qualitatively by local resolution, calculated in cryoSPARC v2.

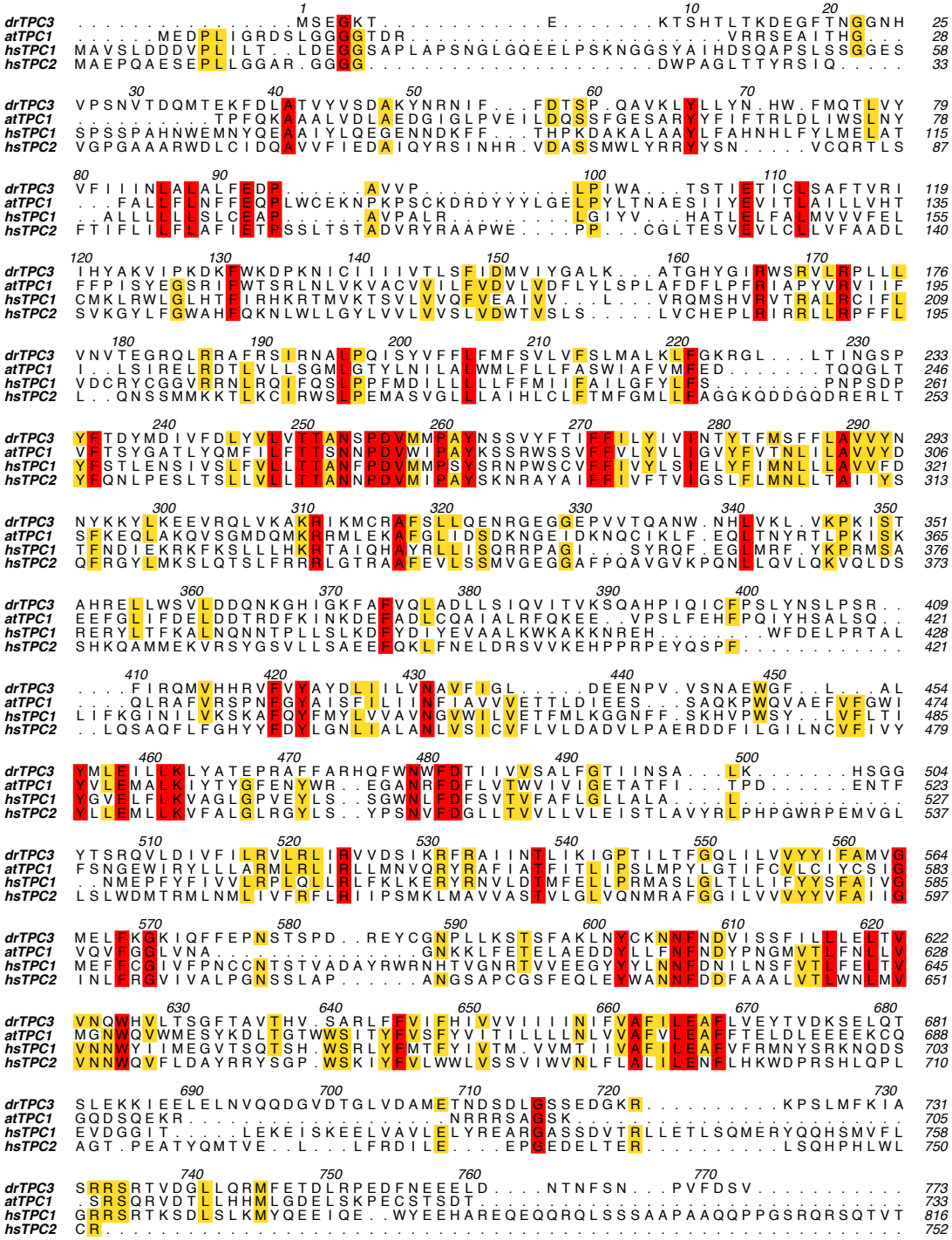

SFig. 1.5: Global sequence alignment of zebrafish TPC3 (DrTPC3); *Arabidopsis thaliana* TPC1 (AtTPC1); human TPC1 (HsTPC1); and human TPC2 (HsTPC2).

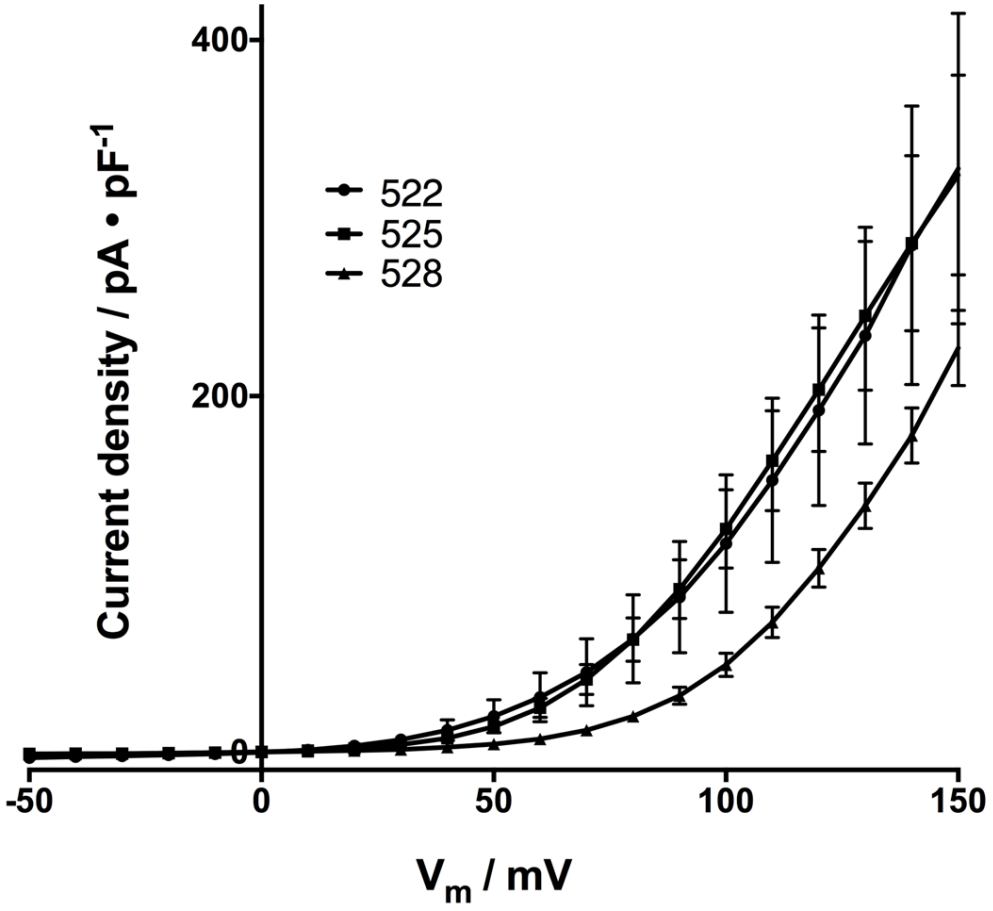

SFig. 1.6: Current densities of the R-Q amino acid substitutions in VSD2.

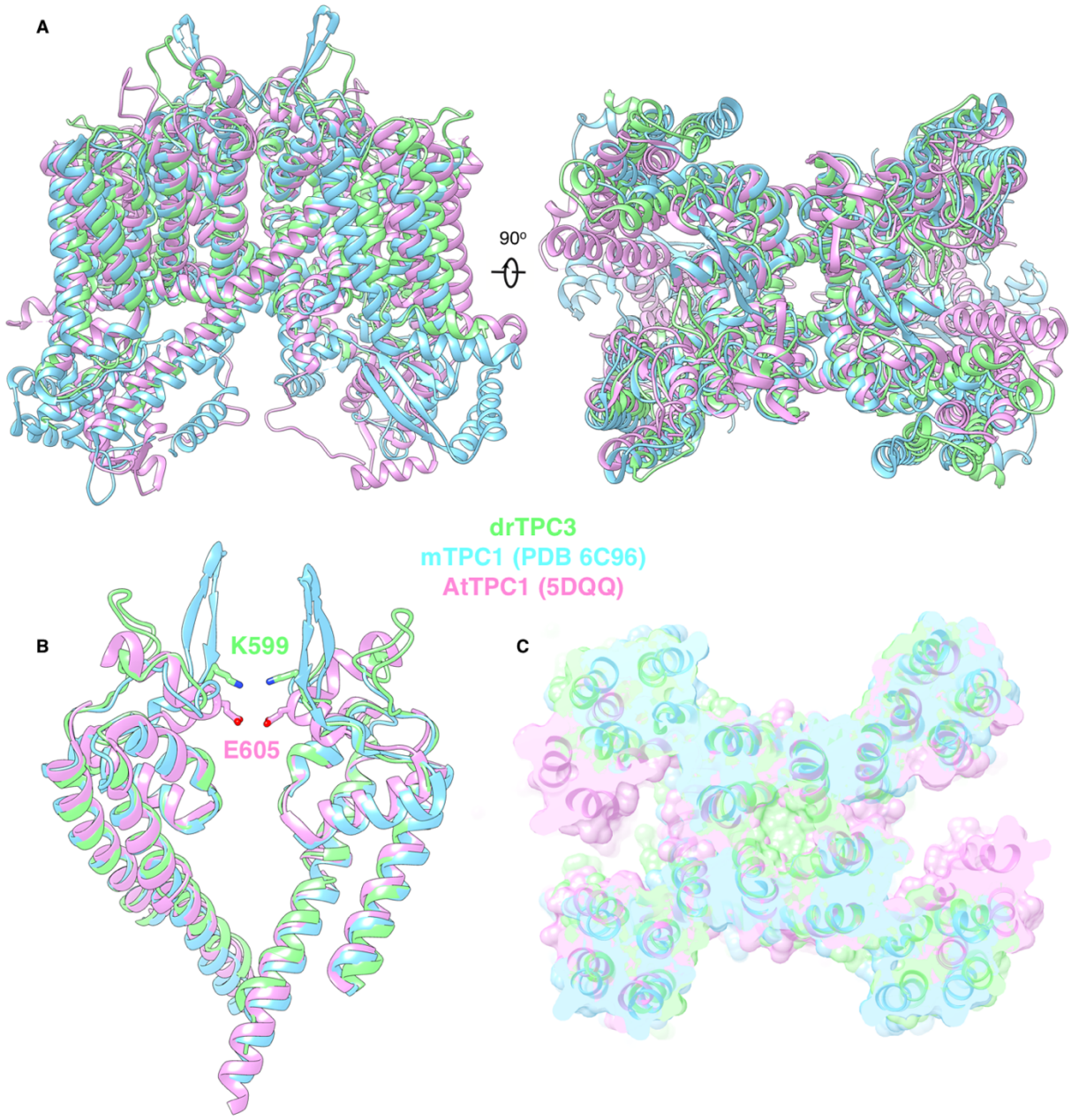

SFig. 1.7: **(A)** Global comparison of drTPC3, mTPC1 and atTPC1 illustrated by orthogonal views. **(B)** Comparison of the pore vestibule formed in filter 2 across TPCs. **(C)** Surface views shown to emphasize the different orientations of VSD2 across TPCs with respect to the rest of the channel.

STable 1: EM refinement and modeling statistics

Microscopy data collection	
Microscope	Titan Krios
Camera	K2 Summit
Illumination mode	Nanoprobe, ~ 1.3 µm IA
Camera mode	Super-resolution
Voltage	300 kV
Pixel size (super-resolution)	0.407 Å pix^{-1}
Underfocus range	0.8 - 2.0 µm
Electron dose	92 e^{-} $Å^{-2}$
Exposure time	10 s
Frames per image	100
Images collected	7221
Image processing	
Software	Relion, cisTEM, cryoSPARC
Autopicked particles	1,201,080
No. particles post 2D classification	706,801
No. particles in final reconstruction	170,446
Resolution (FSC, 0.143 cutoff)	3.3 Å (cisTEM), 3.1 Å (cryoSPARC)
B-factor for sharpening	-90 $Å^2$ (cisTEM), local sharpening (cryoSPARC)
Model statistics	
Map to model resolution (FSC, 0.5 cutoff)	3.3 Å
No. atoms	8893
No. residues	1088
Ramachandran favored	90.52 %
Ramachandran allowed	9.11 %
Ramachandran outliers	0.37 %
MolProbity score	2.84
RMS bond length	0.008 Å
RMS bond angles	0.830 degrees

Chapter 2

Large-scale motions define the voltage gating of an ion channel TPC1

Abstract

Voltage-gated ion channels confer excitability to biological membranes, initiating and propagating electrical signals across large distances on short time scales. Membrane excitation requires channels that respond to changes in electric field and couple the transmembrane voltage to gating of a central pore. To address the mechanism of this process in a voltage gated ion channel, we determined the structures of the ion channel TPC1 at different stages along its voltage-activation pathway. These high-resolution structures of intermediately- and fully-activated electrical states, when compared with the resting state structure, portray a mechanism in which the voltage-sensing domains undergo dilation, and in-membrane plane rotation about the gating charge-bearing helix, followed by charge translocation across the charge transfer seal. The structures, in concert with patch clamp electrophysiology, show that residues in the pore mouth which influence sensitivity to inhibitory Ca^{2+} are allosterically coupled to the voltage sensor and form a secondary gate within the conduction pathway. These conformational changes constitute a new insight into the mechanism of voltage-sensor domain activation in which activation occurs vectorially over a series of elementary steps.

Introduction

Voltage-gated ion channels (VGICs) use voltage sensing domains (VSD) to sense the change in electrical potential across biological membranes (*1*, *2*) and alter the

open probability of a central channel. VSDs are typically peripheral to, but in contact with a single central pore. They are composed of a four helix bundle, in which one helix carries charged residues that move in response to changes in transmembrane electric field (*3*, *4*). Voltage sensors usually adopt a 'resting state' when the membrane is at 'resting potential': ~ -80 mV for animal and ~ -150 mV for plant plasma membranes (*5*). In comparison, much lower resting membrane voltages are set for endo-membranes: ~ -30 mV across the plant vacuole (*6*) and mammalian lysosomal membranes (*7*). As the membrane potential vanishes during depolarization, so does the downwards force on the cationic side chains causing them to move across the membrane (*8*). This conformational change is conveyed to the central pore, usually formed by four pore domains in a quasi four-fold arrangement, which dilates to allow the flow of ions down their electrochemical gradients. The exact nature of this conformational change has been the subject of decades of biophysical investigation (*9*–*12*) though to this date only a few structural examples exist of voltage sensors in multiple conformations (*13*–*18*).

Two-pore channels (TPCs) are defined by their tandem *Shaker* cassette subunits, which dimerize to form a C2-symmetric channel with 24 (4x6) transmembrane helices (Fig. 1E) (*19*–*21*). Each polypeptide chain therefore contains two copies of a voltage sensing and pore domain. Once dimerized, they subunits are arranged in a domain-swapped manner such that the N-terminal VSD (VSD1) contacts the C-terminal pore forming domain of the same chain (Fig. 1C). Likewise, the C-terminal VSD (VSD2) lies against the N-terminal pore forming domain of the second protein chain. There are three TPC channels, TPC1, 2, and 3, each with different voltage or ligand gating, and

ion selectivity. Among the voltage-gated TPCs (all except TPC2 that is lipid gated), only the second VSD (VSD2) is electrically active (*18*, *22*–*24*) whereas VSD1 is probably static under all changes in potential.

In plants, the vacuole comprises up to 90% of the plant cell volume and provides for a dynamic storage organelle that besides metabolites, is a repository for ions including Ca^{2+}. TPC1 channels confer excitability to this intracellular organelle (*25*) and, unlike other TPCs, are calcium regulated: external Ca^{2+} concentration (in the vacuolar lumen) inhibits the channel by acting directly on the extracellular side of VSD2. In contrast, cytosolic Ca^{2+} is required to activate the channel by binding to EF-hands (*22*). These properties allowed our group and Youxing Jiang's to determine the first structure of an electrically resting VGIC by co-crystallizing the channel with 1mM Ca^{2+} (*16*, *22*).

In order to visualize activated states, here we used a well-known gain-of-function mutant in plant TPC1, D454N termed *fou2*, that desensitizes the channel to inhibitory, external (luminal) calcium ions (*26*, *27*). This single amino acid substitution, D454N, lies in the coordination sphere of the inhibitory Ca^{2+} site on the luminal side of VSD2 (Fig. 1C). In plants, this mutation enhances the defense capacity against fungal or herbivore attack due to increased production of the wounding hormone jasmonate (*28*). These effects on plant performance and defense are probably due to short circuiting of the vacuolar membrane (*26*, *27*, *29*) in which TPC1 has increased open probability at the resting potential. Compared to wild type TPC1, the activation threshold in the *fou2* channel is shifted to more negatively polarized potentials. The *fou2* channel also has

significantly lower sensitivity to inhibitory Ca^{2+}, and exhibits faster activation kinetics than its WT counterpart, originally named the “slow vacuolar” (SV) channel due to its slow conductance onset (*20*, *21*, *29, 30*). Therefore, D454N confers more than just reduced Ca^{2+} sensitivity, but overall hyperactivity as well. By determining structures of AtTPC1 D454N in the presence and absence of Ca^{2+}, we explain these unique electrophysiological properties and elucidate the complete electrical activation process in this channel.

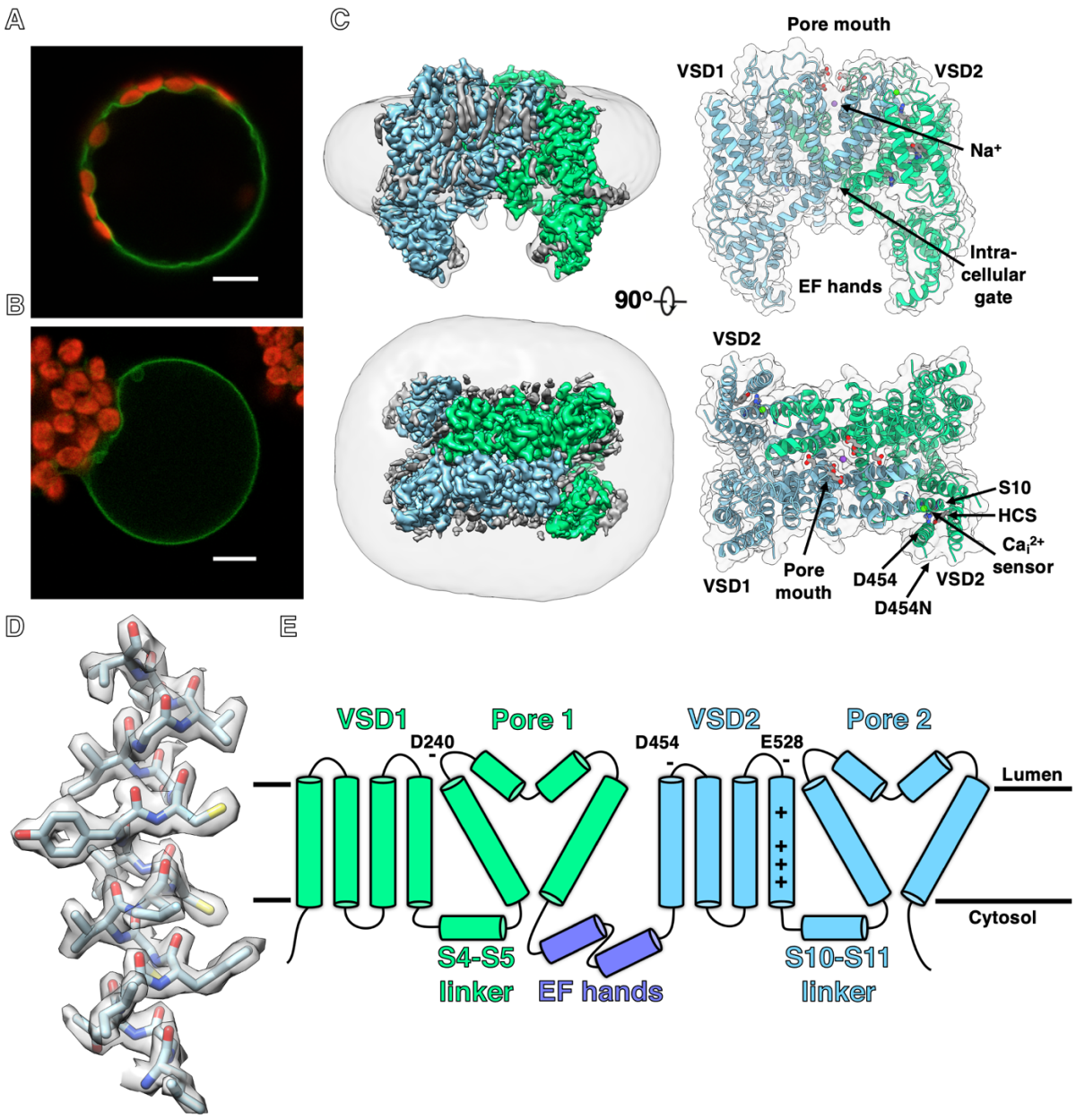

Figure 2.1. CryoEM structure of the vacuolar two-pore channel 1 D454N at atomic resolution: (A) Confocal fluorescent image of an Arabidopsis leaf protoplast released from the TPC1 loss-of-function mutant *tpc1-2* expressing a TPC1-GFP construct. **(B)** Confocal fluorescent image of the vacuole liberated by selective hypo-osmotic shock from a protoplast depicted in (A). In **(A, B)** red fluorescence results from chlorophyll auto-fluorescence of chloroplasts; scale bar = 10 µm. **(C)** Orthogonal views of the Ca^{2+}-bound, unsharpened Coulomb potential map, colored by subunit. A low pass filtered map is shown to approximate the boundaries of the detergent micelle. Lipidic densities are shown in grey. The atomic model is shown with functionally relevant side-chains, namely the acidic residues in the pore mouth and the gating charges and hydrophobic seal within the charge transfer center. **(D)** Atomic detail in the potential map obtained after density

modification, showing the quality of the fitted structure. **(E)** 2D schematic of the tandem *Shaker* cassette subunit that defines the two-pore channel polypeptide. The locations of the acidic residues that constitute the VSD2 Ca_i^{2+}-sensor are shown with **-** symbols.

Results

To test whether wild type and mutant TPC1 channels generated are properly targeted in the plant cell, leaf protoplasts (mesophyll cells with removed cell wall) from Arabidopsis plants (Fig. 1A) were transiently transformed with C-terminal GFP-tagged versions of the plant two-pore channel 1. Upon selective osmotic disruption of the plasma membrane (*31*) the green fluorescence of TPC1-GFP expressing vacuoles (Fig. 1B, Fig. S1A) is visible and their vacuolar membrane accessible for patch clamp electrophysiology (Fig. 4). For structural inspection of wild type TPC1 and the hyperactive *fou2* mutant channel, we used high resolution cryogenic electron microscopy (Fig. 1C). We asked how the voltage sensing domain from this plant vacuolar TPC1 channel evolves during membrane depolarization and what structural changes occur to activate the channel. To this end, we prepared the channel for single particle analysis by vacuolar expression in *Saccharomyces cerevisiae* and purification using the gentle detergent glycodiosgenin (Fig. S2).

D454 controls compactness of the voltage sensing domain

In the presence of 1 mM Ca^{2+}, the *fou2* D454N channel binds Ca^{2+} via the two other carboxylate residues that remain in the wild-type chelation site, namely D240 from the N-terminal pore domain (of the other protein chain) and E528 from the gating-charge-bearing S10 helix (Fig. 2A). Loss of the acidic residue on S7 of VSD2 causes the helix to move away from the charge transfer center, and subsequent shifting of S8

and S9 causes dilation of the VSD (Fig. 2A). This subtle structural rearrangement results in a slightly more relaxed four helix bundle, indicating that the luminal Ca^{2+} site controls domain constriction. This less sterically hindered conformation of the VSD may explain the mutant's fast activation. Accompanying this conformational change is a full 180^{o} rotation of the luminal residues on S10 due to a 3_{10} to α-helix transition, causing R531 to move from interacting with E511 to E468. Despite these differences, the gating charges (R3-R5 in the *Shaker* convention) located along the S10 helix are still in the 'down state', overlaying almost exactly with those in the WT crystal structure (Fig. 2A). Therefore, D454N does not ablate inhibition by external Ca^{2+} but rather primes the channel for activation by unlocking S7 from the VSD-pore interface.

The VSD Ca^{2+} binding site forms a hinge with the pore

Removal of Ca^{2+} renders the channel much more dynamic. In the presence of the calcium chelator EDTA the D454N channel adopts multiple states that can be visualized at low resolution by 3D classification. VSD2 is particularly mobile and moves laterally in the membrane plane, rotating as a rigid body around the axis of the gating charge helix S10. Multiple rounds of 3D classification converged on three discrete states (Fig. 2B). The first of these appears at highest resolution and is seemingly identical to the wild-type, external Ca^{2+}-bound structure.

The second conformation at medium resolution and the third at low resolution exhibit significant conformational differences from the native Ca^{2+}-bound structure, where the VSD2 helices have rotationally shifted by ~ 10 Å. Iterative refinement of the

second conformation yielded a map of suitable quality to determine the structure of VSD2, with a global resolution of ~ 2.8 Å, and a local VSD2 resolution of ~ 3.8 Å. This conformation shows that the gating charges have moved ~ 7 Å upwards along with their alpha-carbons by approximately one helical turn, so that the charges cross the hydrophobic constriction site (HCS) formed by Y475. In a unique fashion, R543 (R5 in the *Shaker* convention), has rotated out of the four helix bundle, to point more towards the pore (Fig. 2C). This demonstrates that the gating charges translocate upwards, in contrast to previously suggested mechanisms (*17*), although dynamics in the entire voltage sensing domain do seem to play an integral part in activation. These dynamics may explain in part why sufficiently high resolution in VSD2 was not previously achievable. The distribution of images between the three states recovered from the EDTA dataset is likely indicative of the actual proportions of microstates in the ensemble of particles present at 0 mV potential. The approximate distribution of particle images between states I:II:III is 10:1:1, indicating that the energetic differences between the states is on the order of ~ 1.5 kcal mol^{-1}.

Overall, S10 moves only subtly between the resting and voltage-activated structures, whereas the other three helices in the bundle move substantially in the membrane plane. Y475 (that forms the hydrophobic seal of the charge transfer center, termed HCS) moves by ~ 5 Å in the membrane plane, probably to prevent a steric clash with R4 and R5 during translocation (Fig. 2C). These data suggest that the electrical activation process in AtTPC1 differs from all other structurally-characterized VGIC mechanisms: large scale conformational changes in the VSD precede charge

translocation. Whether or not this is a general mechanism amongst VGICs will become apparent as more channel structures are determined along their respective activation coordinates.

We conclude that D454 controls internal compactness of the VSD, while D240 (from the pore) and E528 (from VSD2) form the hinge between the VSD2 and the pore - and the angle formed at this hinge depends on the presence of Ca_i^{2+}. In the presence of Ca_i^{2+}, the VSD is poised inwards, locked in place by a chelate involving both domains while removal of the Ca_i^{2+} allows the VSD to move in-plane, sampling multiple discrete states. When in the outwardly poised state (i.e. the channel is more quasi-C4 symmetric) and the membrane potential has sufficiently depolarized, the S10 helix can activate, during which the gating charges translocate upwards to access extracellular solvent (Fig. 2C). This mode of activation is consistent with some proposed mechanisms based on crystal structures of the bacterial Na^+ channels Na_VRh and Na_VAb, which differ by large shifts in the VSD region despite a near-perfectly overlaid pore domain (*32*–*35*). Furthermore, the azimuthal angle formed between the VSD and pore domains of TPC3 (*18*) and murine TPC1 (*36*) show that VSD mobility across the two-pore channel family may be an essential component of channel activation, and that electromechanical coupling may consist of more complex motions than the ‘tug’ at the S4-S5 linker.

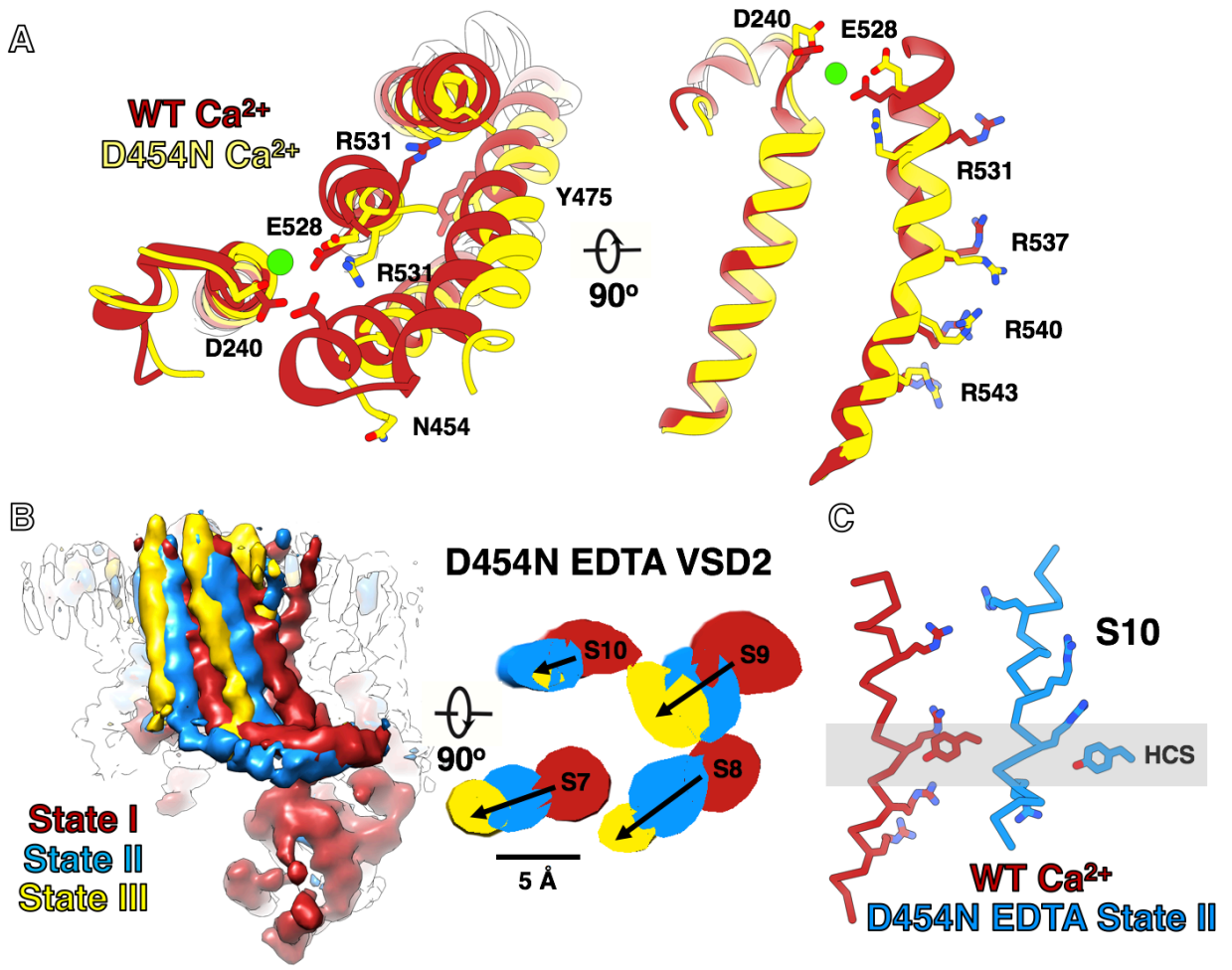

Figure 2.2) Conformational flexibility in VSD2 and charge transfer during voltage activation: (A) Structural comparison of VSD2 between the WT crystal structure (PDB: 5DQQ) and D454N Ca^{2+}, showing dilation of the four helix bundle and HCS, loss of 3_{10} helicity at the luminal side of S10, and remodeling of the Ca_i^{2+} site. Ca^{2+} atoms are shown as green spheres. **(B)** Three conformations of VSD2 are observed from 3D classification of the D454N EDTA dataset, shown here as the unsharpened Coulomb potential maps. State I is most similar to the Ca^{2+} dataset and state III is most distinct. A slice through the four helix bundle parallel to the membrane plane, showing the trajectories of each helix during activation. **(C)** Charge translocation in S10 is defined by a combination of upwards translation and helical screw type motion, accompanied by retraction of the hydrophobic constriction site, Y475.

While all animal TPCs are Na^+-selective, plant TPC1 conducts K^+, Na^+ and Ca^{2+} and this lack of cation discretion is conferred by its quasi-four-fold selectivity filter, with two filter II (from the second pore domain) residues M629 and G630 abolishing Na^+-selectivity (*22*, *23*, *36*, *37*) (Fig. 3A, B). Our structure reveals a detailed arrangement of

waters around a single metal cation bound in the selectivity filter, demonstrating exactly how permeant ions interact with the conduction pathway (Fig. 3C, D). The pore domain of the mutant Ca^{2+} and EDTA channels has completely reorganized, making and breaking contacts relative to the crystal structure of AtTPC1. In comparison to our WT TPC1 structure (PDB: 5DQQ), N631 in filter II has rotated 90^{o} to avoid interacting with its symmetry mate across the pore (Fig. 3B). The hydroxyl of Y608 is repositioned 11 Å to contact the water network around the sodium ion, and D606 is moved by 4 Å into the central water network. In the WT crystal structure, the two-fold symmetry related E605 pair forms the constriction point of the pore mouth, situated above the selectivity filter, and bound a Yb^{2+} ion (a Ca^{2+} mimetic used for phase determination). In D454N, as in the triply-mutated 'DDE' structure in which all three carboxylate (D240N, D4545N, E528Q) residues that form the luminal Ca^{2+} coordination sphere are replaced by amides (*17*), E605 is removed from the conduction pathway, significantly altering the topology and electrostatics of the mouth (Fig. 3B, 3E). D606 in D454N moves to occupy roughly the same position as E605 in the WT structure, indicating that 606 can "replace" the function of E605 when E605 is neutralized (Fig. 3B, 3E).

Interestingly, F611 also moves to displace another Ca^{2+} ion observed in the WT crystal structure between N612 and N625. It has been proposed that there are inhibitory Ca^{2+} sites in the pore domain of AtTPC1 (*20*), so these rearrangements may alleviate Ca^{2+} inhibition at the pore. In summary we conclude that the Ca^{2+}-dependent positioning of D454 is allosterically coupled to the pore and that the insensitivity of *fou2* (D454N) to luminal Ca^{2+} is manifest in three locations. Therefore, the diminished sensitivity to

luminal, inhibitory Ca^{2+} in the *fou2* channel can be explained by these conformational changes which clearly show that Ca^{2+}-binding sites are remodeled to exclude Ca^{2+} at multiple sites across the channel's luminal face.

The pore mouth influences voltage and luminal Ca^{2+} sensing

In order to determine what functional effect the pore mouth has on channel activation, we made substitutions in E605Q, D606N and D607N (Fig 3) and transiently transformed protoplasts of the TPC1 loss-of-function mutant *tpc1-2* with individual single and triple mutant SV channels (Fig. 1A). Patch-clamp measurements with isolated vacuoles (Fig. S1A) were performed in the whole-vacuole configuration. Typical macroscopic, outward-rectifying TPC1 currents were recorded in response to membrane depolarization (Fig. S1B, C). Raising the luminal Ca^{2+} concentration from 0 to 10 mM affected both ion channel current amplitude (Fig. S1B, C) and voltage dependent properties (Fig. 4). As a proxy for the latter, we displayed the voltage-dependent relative open channel probability (Fig. 4A). To our surprise, mutating the negatively charged residues impacted channel function in two ways. First, in the absence of luminal Ca^{2+} the open probability of the single mutant channels E605A, or D606N shifted significantly towards more negatively polarized membrane potentials (Fig. 4B). This implies that the luminal pore mouth is directly coupled to voltage sensing. Second, neutralization of all three amino acids together (E605Q/D606N/D607N) further reduced the susceptibility to inhibitory luminal Ca^{2+} (Fig. 4C). Hence the conformational changes we observe in the pore mouth between the resting, closed WT channel and the activated D454N channel

are functionally relevant and suggest that the negatively charged cluster at the external entrance to the pore (605-607) are involved in channel gating.

Since the TPC1 channel is a non-selective cation channel, the observed ion in the selectivity filter could be either Na^+ or Ca^{2+} (K^+ is absent in the buffer). We assign the density to Na^+ since the buffer consists of a 200-fold excess of Na^+ (200 mM vs 1 mM), though the putative coordination geometry is favorable for either ion (*1*, *38–40*), and the ionic radii of Na^+ and Ca^{2+} (1.16 Å and 1.14 Å, respectively) are almost identical. The amide carbonyl to metal distance is 2.3 Å and the equatorial water to metal distance is 2.5 Å. We used the 'CheckMyMetal' server (*41*) to validate the consistency of ions in this position. The coordination geometry is almost octahedral, though the lower axial water to ion distance is 2.9 Å.

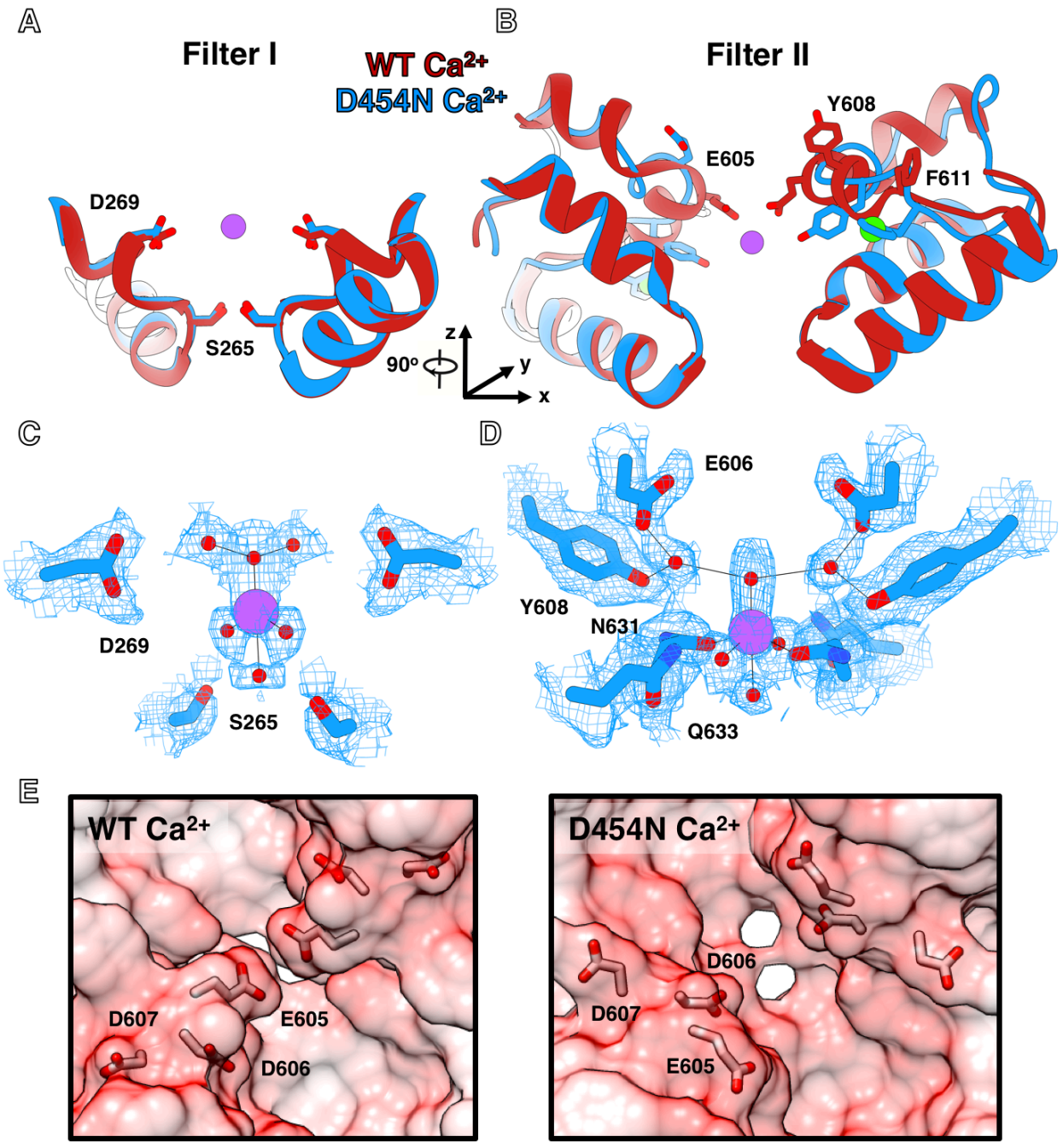

Figure 2.3) Conformational changes in the pore domain between AtTPC1 WT and D454N: (A) Overlay of WT AtTPC1 (red, PDB: 5DQQ) and D454N (blue) showing no perturbations in filter I due to the mutation. The channel axes are shown where z is coincident with the pore, and the xy plane is parallel with the membrane. **(B)** Large conformational changes in the metal and water binding pore residues in filter II along with exclusion of a proximal Ca^{2+} ion by F611. **(C)** Sharpened potential map zoned 2 Å around atoms of interest showing hydration around the bound metal and interactions with filter I. **(D)** Same as **(C)** but from the perspective of filter II. **(E)** Coulombic surface representation of the pore mouth of WT (left) and D454N (right) showing how rearrangements in the

three acidic residues 605-607 alter the topology of the region. The viewing direction is in parallel with the pore axis.

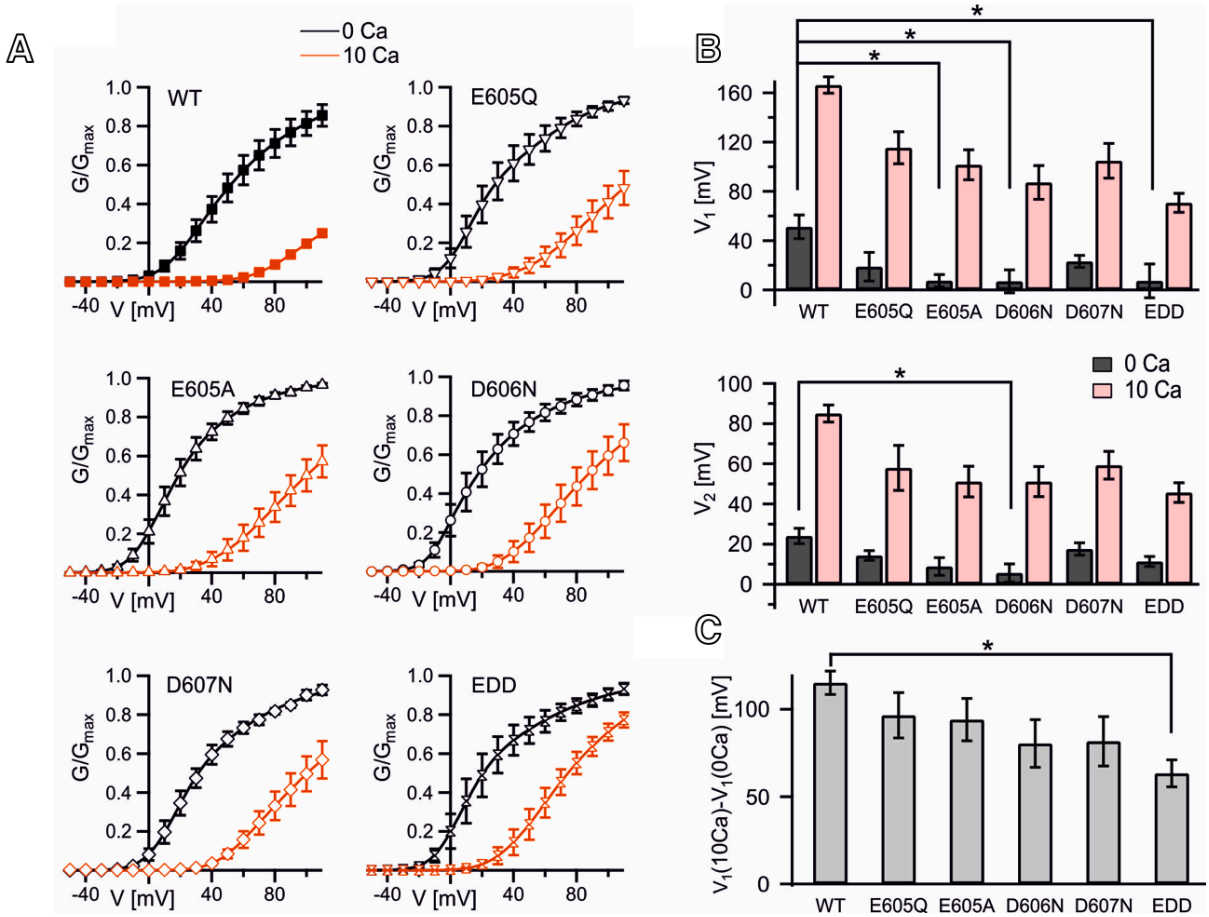

Figure 2.4) The pore mouth operates a luminal Ca^{2+} sensor functionally coupled to the voltage sensor: (A) Normalized conductance-voltage plots ($G/G_{max}(V)$) of WT and pore mouth mutants in the presence (red symbols and line, 10 mM Ca^{2+}) and absence (black symbols and line) of luminal Ca^{2+}. Symbols represent means ± SE, and solid lines provide the best fits of the G(V) plots to a double Boltzmann function. **(B)** Half-activation voltages V_1 and V_2 given as means ± SE in the presence of 0 and 10 mM Ca^{2+} in the vacuole lumen. $V_{1/2}$ values were derived from the double Boltzmann fits of the G(V) plots shown in **(A)**. Significant differences were only analyzed for $V_{1/2}$ values under luminal Ca^{2+}-free conditions with one-way ANOVA followed by Tukey's post hoc comparison test and indicated by asterisks (*p < 0.05). **(C)** Changes in V_1 values upon a rise in luminal Ca^{2+} from 0 to 10 mM. Asterisks indicate significant differences (*p < 0.05, one-way ANOVA with Tukey's post hoc comparison test). Note, Ca^{2+}-induced changes in V_2 values for all channel variants are summarized in Table S1. In **(A-C)** the number of experiments performed on individual vacuoles per channel variant was n=5 for WT, E605Q, E605A, D606N and n=4 for D607N and EDD under luminal Ca^{2+}-free conditions. For 10 mM

luminal Ca^{2+}, the number of experiments was n=5 for WT, E605Q and n=4 for E605A, D606N, D607N and EDD. EDD represents the triple TPC1 mutant E605Q/D606N/D607N.

Discussion

We used cryo-EM to define the activation cycle of a voltage-gated ion channel. Our structures show that the voltage sensor undergoes a number of discrete steps along it's activation coordinate including dilation, in-plane rotation and finally charge translocation, in that order. Furthermore, we show that the VSDs are coupled to a novel luminal Ca^{2+} sensor within the conduction pathway, termed the "pore mouth", and that the conformational changes we observe in that region are functionally relevant. This gating at the pore mouth functions in addition to steric gating at the canonical intracellular activation gate.

The *fou2* channel has previously been shown to have faster activation kinetics, and altered voltage- and calcium-dependent gating compared to the wild type channel (26, 28). Our data here allow us to propose two reasons for these observations. First, dilation of the VSD lowers the energetic barrier to gating charge translocation across the hydrophobic constriction site, resulting in the observed faster voltage-dependent activation. Second, significant conformational changes in the external mouth of the pore decrease the resistance of the conduction pathway, likely through steric effects and complex interactions with the extracellular hydration network. These conformational changes in the pore mouth reflect allosteric communication from the VSD, that are apparently not conveyed through the S10-S11 linker since it remains unchanged structurally, but rather through subtle rearrangements near the VSD2 Ca^{2+} site. Therefore, the D454 position, given its placement between VSD2 and the central pore,

represents an important regulatory site in the luminal face of the channel that interacts with external Ca^{2+}, disruption of which has allosteric implications across the pore domain to include altering distal Ca^{2+}-binding sites across the channel.

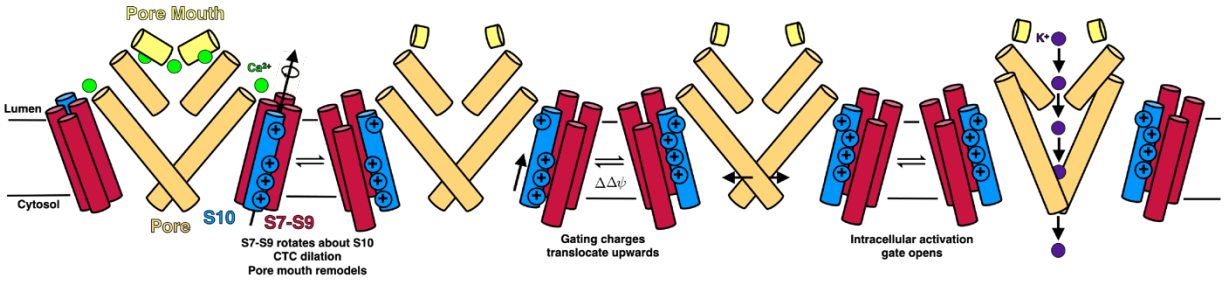

Figure 2.5) Proposed mechanism of AtTPC1 voltage activation: In the presence of luminal Ca^{2+} (Ca_i^{2+}), the VSD is compact and the gating charges are in the 'down' position (as represented in the WT crystal structure PDB: 5DQQ) (left). Removal of luminal Ca^{2+} dilates the CTC and S7-S9 move rotationally clockwise if viewed from the outside, around S10, adopting states I-III (moving to the right) as described in figure 2B. This flexibility in the VSD is coupled to conformational change in the pore mouth that transitions between a Ca^{2+}-binding competent and incompetent state. If the membrane potential is sufficiently depolarized, the gating charges will translocate upwards into their electrically active state. While in the electrically-activated state, the intracellular activation gate can open when the cytosolic EF-hands are loaded with Ca^{2+}.

Using image processing, we determined multiple structures of sparsely populated states of a dynamic voltage-gated ion channel, allowing us to describe a novel mechanism for a multi-step voltage-dependent activation. Further analysis will reveal whether similar processes occur in other voltage-gated ion channels, many of whose structures are currently limited to determination of a single voltage-dependent state (*18*, *23*, *36*), where elusive and dynamic processes may be responsible for the multitude of previously proposed, often conflicting mechanisms of voltage activation.

Acknowledgements

We thank David Bulkley, Zanlin Yu and Glen Gilbert for their maintenance of the UCSF EM core, and the NIH grants that support it. The research was funded by NIH Grant R01 GM24485 (to R.M.S.). Patch clamp studies were supported by the Koselleck award to R.H. (HE1640/42-1) from the German Research Foundation (DFG). M.S.D. acknowledges a NSF graduate research fellowship. J.L. is grateful for a doctoral fellowship from the China Scholarship Council. We thank Erwin Neher for discussion and vision. We thank Paul Thomas, Daniel Asarnow and Matt Harrington for computational assistance, Joshua Baker-LePain for his maintenance of the UCSF HPC cluster and Dietmar Geiger for his support in primer design.

Author contributions

M.S.D. and J.L. performed experiments; M.S.D., J.L., I.M., R.H. and R.M.S. designed experiments, analyzed data and wrote the manuscript.

Declaration of interests

The authors declare no competing interests.

Data availability

The unfiltered and unmasked half maps, unsharpened reconstructions, locally sharpened reconstructions for both datasets, and density modified Ca^{2+}-bound reconstruction will soon be available in the Electron Microscopy Data Bank (EMDB).

REFERENCES

1. W. A. Catterall, G. Wisedchaisri, N. Zheng, The chemical basis for electrical signaling. *Nat. Chem. Biol.* **13**, 455–463 (2017).
2. C. Miller, Ionic channels of excitable membranes.: By Bertil Hille. Sunderland, Massachusetts: Sinauer.(1991). 607 pp. $46.95 (1992).
3. A. L. Hodgkin, A. F. Huxley, A quantitative description of membrane current and its application to conduction and excitation in nerve. *J. Physiol. (Lond.)*. **117**, 500–544 (1952).
4. F. Bezanilla, How membrane proteins sense voltage. *Nat. Rev. Mol. Cell Biol.* **9**, 323–332 (2008).
5. R. Hedrich, Ion channels in plants. *Physiol. Rev.* **92**, 1777–1811 (2012).
6. Y. Wang *et al.*, Cytosolic ca(2+) signals enhance the vacuolar ion conductivity of bulging arabidopsis root hair cells. *Mol. Plant*. **8**, 1665–1674 (2015).
7. H. Xu, D. Ren, Lysosomal physiology. *Annu. Rev. Physiol.* **77**, 57–80 (2015).
8. F. Bezanilla, Gating currents. *J. Gen. Physiol.* **150**, 911–932 (2018).
9. J. Payandeh, D. L. Minor, Bacterial voltage-gated sodium channels (BacNa(V)s) from the soil, sea, and salt lakes enlighten molecular mechanisms of electrical signaling and pharmacology in the brain and heart. *J. Mol. Biol.* **427**, 3–30 (2015).
10. G. Dai, T. K. Aman, F. DiMaio, W. N. Zagotta, The HCN channel voltage sensor undergoes a large downward motion during hyperpolarization. *Nat. Struct. Mol. Biol.* **26**, 686–694 (2019).
11. B. Chanda, O. K. Asamoah, R. Blunck, B. Roux, F. Bezanilla, Gating charge displacement in voltage-gated ion channels involves limited transmembrane

movement. *Nature*. **436**, 852–856 (2005).

12. K. S. Glauner, L. M. Mannuzzu, C. S. Gandhi, E. Y. Isacoff, Spectroscopic mapping of voltage sensor movement in the Shaker potassium channel. *Nature*. **402**, 813–817 (1999).
13. H. Xu *et al.*, Structural Basis of Nav1.7 Inhibition by a Gating-Modifier Spider Toxin. *Cell*. **176**, 1238–1239 (2019).
14. T. Clairfeuille *et al.*, Structural basis of α-scorpion toxin action on Nav channels. *Science*. **363** (2019), doi:10.1126/science.aav8573.
15. G. Wisedchaisri *et al.*, Resting-State Structure and Gating Mechanism of a Voltage-Gated Sodium Channel. *Cell*. **178**, 993–1003.e12 (2019).
16. A. F. Kintzer, R. M. Stroud, Structure, inhibition and regulation of two-pore channel TPC1 from Arabidopsis thaliana. *Nature*. **531**, 258–262 (2016).
17. A. F. Kintzer *et al.*, Structural basis for activation of voltage sensor domains in an ion channel TPC1. *Proc. Natl. Acad. Sci. USA*. **115**, E9095–E9104 (2018).
18. M. S. Dickinson, A. Myasnikov, J. Eriksen, N. Poweleit, R. M. Stroud, Resting state structure of the hyperdepolarization activated two-pore channel 3. *Proc. Natl. Acad. Sci. USA*. **117**, 1988–1993 (2020).
19. A. F. Kintzer, R. M. Stroud, On the structure and mechanism of two-pore channels. *FEBS J.* **285**, 233–243 (2018).
20. R. Hedrich, T. D. Mueller, D. Becker, I. Marten, Structure and function of TPC1 vacuole SV channel gains shape. *Mol. Plant*. **11**, 764–775 (2018).
21. R. Hedrich, I. Marten, TPC1-SV channels gain shape. *Mol. Plant*. **4**, 428–441 (2011).

22. J. Guo *et al.*, Structure of the voltage-gated two-pore channel TPC1 from Arabidopsis thaliana. *Nature*. **531**, 196–201 (2016).

23. J. She *et al.*, Structural mechanisms of phospholipid activation of the human TPC2 channel. *Elife*. **8** (2019), doi:10.7554/eLife.45222.

24. D. Jaślan *et al.*, Gating of the two-pore cation channel AtTPC1 in the plant vacuole is based on a single voltage-sensing domain. *Plant Biol. (Stuttg.)*. **18**, 750–760 (2016).

25. D. Jaślan *et al.*, Voltage-dependent gating of SV channel TPC1 confers vacuole excitability. *Nat. Commun.* **10**, 2659 (2019).

26. D. Beyhl *et al.*, The fou2 mutation in the major vacuolar cation channel TPC1 confers tolerance to inhibitory luminal calcium. *Plant J.* **58**, 715–723 (2009).

27. B. Dadacz-Narloch *et al.*, A novel calcium binding site in the slow vacuolar cation channel TPC1 senses luminal calcium levels. *Plant Cell*. **23**, 2696–2707 (2011).

28. G. Bonaventure *et al.*, A gain-of-function allele of TPC1 activates oxylipin biogenesis after leaf wounding in Arabidopsis. *Plant J.* **49**, 889–898 (2007).

29. A. Lenglet *et al.*, Control of basal jasmonate signalling and defence through modulation of intracellular cation flux capacity. *New Phytol.* **216**, 1161–1169 (2017).

30. R. Hedrich, E. Neher, Cytoplasmic calcium regulates voltage-dependent ion channels in plant vacuoles. *Nature* (1987).

31. B. Schulz-Lessdorf *et al.*, Coordination of plasma membrane and vacuolar membrane ion channels during stomatal movement. *Symp Soc Exp Biol*. **48**, 99–112 (1994).

32. C. A. Ahern, J. Payandeh, F. Bosmans, B. Chanda, The hitchhiker's guide to the voltage-gated sodium channel galaxy. *J. Gen. Physiol.* **147**, 1–24 (2016).

33. X. Zhang, N. Yan, The conformational shifts of the voltage sensing domains between Na(v)Rh and Na(v)Ab. *Cell Res.* **23**, 444–447 (2013).

34. J. Payandeh, T. M. Gamal El-Din, T. Scheuer, N. Zheng, W. A. Catterall, Crystal structure of a voltage-gated sodium channel in two potentially inactivated states. *Nature*. **486**, 135–139 (2012).

35. X. Zhang *et al.*, Crystal structure of an orthologue of the NaChBac voltage-gated sodium channel. *Nature*. **486**, 130–134 (2012).

36. J. She *et al.*, Structural insights into the voltage and phospholipid activation of the mammalian TPC1 channel. *Nature*. **556**, 130–134 (2018).

37. J. Guo, W. Zeng, Y. Jiang, Tuning the ion selectivity of two-pore channels. *Proc. Natl. Acad. Sci. USA*. **114**, 1009–1014 (2017).

38. T. Dudev, C. Lim, Ion selectivity strategies of sodium channel selectivity filters. *Acc. Chem. Res.* **47**, 3580–3587 (2014).

39. T. Dudev, C. Lim, Evolution of eukaryotic ion channels: principles underlying the conversion of Ca^{2+}-selective to Na^{+}-selective channels. *J. Am. Chem. Soc.* **136**, 3553–3559 (2014).

40. E. Gouaux, R. Mackinnon, Principles of selective ion transport in channels and pumps. *Science*. **310**, 1461–1465 (2005).

41. H. Zheng *et al.*, Validation of metal-binding sites in macromolecular structures with the CheckMyMetal web server. *Nat. Protoc.* **9**, 156–170 (2014).

Supplementary materials for chapter 2

Methods

Protein expression and purification

All AtTPC1 constructs were cloned into our 83nu yeast expression vector (*1*) that incorporates a C-terminal 10x His tag preceded by a thrombin cleavage sequence. The plasmids were transformed into DSY5 *Saccharomyces cerevisiae* and grown on SC-His^- plates. A single colony was used to inoculate a 100 mL starter culture of SC-His^- media, and grown overnight at 30°C. The starter culture was used to inoculate 750 mL of SC-His^- media and grown overnight at 30°C. 250 mL of Yeast Extract-Peptone-glycerol (YPG) media was added to induce expression of TPC1 and grown overnight at 30°C. All of the following steps were performed at 4°C. Cells were harvested by centrifugation and resuspended in lysis buffer (50 mM Tris pH 7.5, 500 mM NaCl, 10% glycerol, 1 mM PMSF, 1 protease inhibitor tablet per 100 mL), and lysed by Emulsiflex. The lysate was centrifuged at 16,000 g for 20 minutes to remove debris, then the supernatant was centrifuged at 180,000 g for 1 hr to collect the membrane fraction. Membranes were resuspended in solubilization buffer (50 mM Tris pH 7.5, 200 mM NaCl, 1 mM PMSF, 1 protease inhibitor per 100 mL and 1% β-DDM) such that the membrane mass to volume ratio is 1:20. The suspension was Dounce homogenized and nutated for 2 hr. The suspension was centrifuged at 180,000 g for 30 min to remove un-solubilized material. The supernatant was filtered through a 0.22 μm filter, and 20 mM imidazole was added along with 4 mL Ni^{2+}-NTA resin per 100 mL of lysate volume, and allowed to batch bind for 4-5 hr. The resin was collected on a (disposable) gravity column and washed with

protein buffer (50 mM Tris pH 7.5, 200 mM NaCl and 0.06% glycodiosgenin) first with 20 mM imidazole, then with 75 mM imidazole, then in the absence of imidazole. The washed resin was resuspended in protein buffer and 400 U thrombin was added for overnight, on-resin cleavage. The flow-through was collected, concentrated to 500 µL, and injected onto a Superdex 200 increase 10/300 gel filtration column (GE Healthcare), pre-equilibrated in protein buffer supplemented either with 1 mM EDTA or $CaCl_2$. The peak fraction at ~10 mL (Supp. Fig. 1) was collected and concentrated to ~5 mg mL^{-1} for vitrification.

Microscopy

Freshly glow discharged grids (300 mesh holey carbon Au Quantifoil R1.2/1.3) were used for vitrification in a Mark IV Vitrobot (FEI), using 100% relative humidity and 4 s blot time, and plunge frozen in liquid nitrogen-cooled ethane. The grids were loaded onto an FEI Titan Krios electron microscope operating at 300 kV, equipped with a K3 BioQuantum imaging system, using a 20 eV energy slit. Imaging was performed in nanoprobe mode using a 70 µm C2 aperture, resulting in a ~1.3 µm parallel illuminated area, without an objective aperture. The nominal EFTEM magnification was 105,000x, resulting in a super-resolution pixel size on the specimen of 0.4175 Å pix^{-1}. The dose rate was 8 e^{-} pix^{-1} s^{-1} with a total exposure time of 5.9 s, fractionated into 117 frames, using correlated double sampling. Movies were acquired semi-automatedly with SerialEM (*2*), using 3x3 hole beam-shift image-shift, over a nominal under-focus range of 1.0 to 2.0 µm with focus targeting once per 9 shots. The movies were drift corrected

and dose weighted using UCSF MotionCor2 (*3*) and twice Fourier binned to a pixel size of 0.835 Å pix^{-1}.

Image processing

D454N Ca^{2+}: 4989 dose weighted images (Supp. Fig. 2) were imported into cisTEM (*4*) and CTF fitting was performed using resolutions between 30 and 4 Å. Micrographs with a CTF resolution worse than 5 Å were discarded. $1.2x10^6$ particles were picked *ab initio* in cisTEM, extracted in 432^2 pix^2 boxes and subjected to 2D classification, resulting in $0.55x10^6$ particles from the "good" classes. These particles were then used to calculate a C1 *ab initio* volume in cisTEM which displayed secondary structure. The volume was aligned onto the cyclic symmetry axis using 'relion_align_symmetry', and used as a reference for resolution-limited global angular refinement in cisTEM using C2 symmetry. The resulting map was used to calculate a micelle-excluding, binary mask using 'relion_mask_create', and the particles were subjected to masked local refinement in cisTEM using C2 symmetry. These particles were exported to RELION 3.0 (*5*) for C2 symmetry expansion and 'skip-align' classification, however no asymmetric features were detected. The particle stack was then imported into cryoSPARC v2 (*6*) and subjected to per-particle beam tilt and defocus refinement, followed by non-uniform refinement, yielding a 2.5 Å reconstruction by gold standard Fourier shell correlation using a 0.143 threshold. Un-filtered, un-masked half maps from the refinement were subjected to density modification in Phenix (phenix.resolve_cryo_em) (*7*) which produced a nominally 2.3 Å reconstruction, with clear atomic features.

D454N EDTA: 6685 dose weighted images were imported into cryoSPARC v2 and CTF estimation was performed in patches (Supp. Fig. 3). $1.5x10^6$ particles were picked *ab initio* and extracted in 386^2 pix^2 boxes cropped to 250^2 pix^2. The particles were subjected to 2D classification from which $1x10^6$ "good" particles were selected. These particles were then subjected to global angular refinement against the D454N Ca^{2+} volume, low pass filtered to 30 Å, resulting in a 3.5 Å reconstruction. Although most of the volume was well ordered, VSD2 was poorly resolved. 3D classification into 3 classes showed two distinct classes of VSD2, a high-resolution class similar in conformation to that in the Ca^{2+} structure, and a low-resolution class. Refinement of the particles corresponding to high resolution class yielded a 2.8 Å reconstruction that appears identical to the Ca^{2+} structure. In order to achieve better separation of the VSD2 classes, the entire particle stack before 3D classification was exported to RELION 3.0 (metadata was generated using csparc2star.py from Daniel Asarnow's pyem suite), and a cosine-edged mask comprising only a single VSD2 was calculated using map segmentation in UCSF Chimera followed by relion_mask_create. The metadata were C2 symmetry expanded and subjected to 3D classification in RELION 3.0 without alignment, varying the regularization 'tau parameter' from 10 to 20. Three distinct classes were isolated displaying large conformational differences. The three classes are denoted state I-III, the first of which is the most similar to the D454N Ca^{2+} structure and at highest resolution, and the third of which is the least similar and at lowest resolution. Refinement of state II yielded a promising map at 3.8 Å global resolution, with VSD2 at ~ 4.2-4.5 Å. The particle stack was exported to both cisTEM or cryoSPARC v2 for further refinement. In cisTEM, the particles were subjected to

resolution-limited local refinement in C1, using a micelle-excluding mask in which external signal was not down-weighted but low-pass filtered to 30 Å. After multiple rounds with increasing allowed resolutions, the resulting 3.3 Å map was sharpened using a B-factor of -50 $Å^2$ and used for modeling. In cryoSPARC v2, the particles were subjected to non-uniform local refinement and the map was locally sharpened for model building.

Atomic Modeling

The atomic models were generated using the crystal structures of WT AtTPC1 as reference (PDBs: 5DQQ (*8*) and 5E1J (*9*)) and manipulated in Coot (*10*), followed by iterative rounds of phenix.real_space_refine (*7*) and flexible fitting using Namdinator (*11*). All figures were prepared using UCSF Chimera (*12*).

Plant cultivation

The TPC1 loss-of-function mutant *tpc1-2* from *Arabidopsis thaliana* (*13*) was cultivated in soil for 5-6 weeks in a climate chamber with an 8-h light period and a light intensity of 150 µmol m^{-2} s^{-1}. The temperature in the dark and light was adjusted to 16°C and 22°C, respectively, and the relative humidity was about 60%.

Cloning and mutagenesis procedure

Using the advanced uracil-excision-based cloning technique (*14*, *15*), the cDNA coding sequences for the AtTPC1 channel variants were cloned as C-terminal eGFP fusions (*15*) into the modified pSAT6-eGFP-C1 vector (GenBank AY818377.1), as

essentially described by Dadacz-Narloch *et al*. (*16*). The AtTPC1 channel variants were under the control of the 35S promoter. Site-directed mutations were introduced in wild type AtTPC1 following a modified USER fusion method as described by Dadacz-Narloch *et al.* (*16*). All channel mutants were verified by sequencing. Sequences of all used primers are provided in Table S2.

Transient protoplast transformation

TPC1 channel variants were transiently expressed in mesophyll protoplasts according to a well-established protocol (*17*, *18*). Briefly, for isolation of mesophyll protoplasts the lower epidermis of the leaves was gently scrubbed with sandpaper before incubating the leaves for 3 hr in dark in the enzyme solution (1.5% cellulase R10, 0.4% macerozyme R10, 400 mM mannitol, 20 mM KCl, 20 mM MES, 10 mM $CaCl_2$, 0.1% BSA, pH 5.7 adjusted with Tris). The suspension was then filtered and washed through a 50 µm nylon mesh with 30-40 mL W5 buffer (154 mM NaCl, 125 mM $CaCl_2$, 5 mM KCl, 5 mM glucose, 2 mM MES, pH 5.7 adjusted with Tris) and centrifuged at 100 x *g* for 2 min without acceleration or brake at 4 °C. After removing the supernatant, the enriched protoplasts were incubated on ice for 30 min in W5 to settle at the bottom of the tube. The supernatant was replaced by 5-8 mL MMG solution (4 mM MES pH 5.7, 0.4 M mannitol, 15 mM $MgCl_2$) to obtain about 2 x 10^5 protoplasts per mL MMG. 200 µL protoplast suspension was gently mixed with 20 µg plasmid DNA and 220 µl PEG solution (2 g PEG 4000, 1.5 mL H_2O, 1.25 mL mannitol (800 mM), 0.5 mL $CaCl_2$(1 M)) and incubated for 15 min at room temperature. To stop the reaction, W5 (440 µL) was added to the protoplast suspension. After shaking the tube gently for few seconds, W5

(880 µL) was added for further dilution. Following centrifugation at 100 x *g* for 1 min, the supernatant was removed, and the protoplasts were resuspended and stored in 1.5 mL W5 buffer (plus 50 µg mL^{-1} ampicillin) in the dark and at room temperature for two days.

Fluorescence imaging

To image the correct vacuolar membrane targeting of the TPC1 constructs, the GFP fluorescence signal of transformed protoplasts and vacuoles released therefrom were detected using a confocal laser scanning microscope (TCS SP5, Leica, Mannheim, Germany) (*19*).

Patch clamp experiments

Two days after transformation an aliquot of the protoplast suspension (50 µL) was transferred to the patch-clamp recording chamber and the vacuole-releasing solution was added (250-400 µl VR solution, modified in comparison to that of Lagostena *et al*. (*20*)). The VR-solution was composed of 100 mM malic acid, 155 mM NMDG (N-methyl-D-glucamine), 5 mM EGTA, 3 mM $MgCl_2$, 10 mM Hepes/Tris pH 7.5 and adjusted to 450 $mOsmol \cdot kg^{-1}$ with D-sorbitol. After the whole-vacuole patch-clamp configuration was established with fluorescent vacuoles harboring GFP-tagged TPC1 channels, the VR solution was replaced by the standard bath medium. The bath solution consisted of 150 mM KCl, 1 mM $CaCl_2$, 10 mM Hepes (pH 7.5/Tris) and was adjusted with D-sorbitol to an osmolality of 520 $mOsmol \cdot kg^{-1}$. Patch pipettes with a resistance of 1.5-3.9 MΩ were filled with one of two pipette solutions. Both pipette solutions were composed of 150 mM KCl, 2 mM $MgCl_2$, 10 mM HEPES (pH 7.5/Tris) and adjusted with

D-sorbitol to an osmolality 500 mOsmol·kg^{-1}. One of the pipette solutions additionally contained 0.1 mM EGTA to adjust nominal 0 mM Ca^{2+} (https://somapp.ucdmc.ucdavis.edu/pharmacology/bers/maxchelator/webmaxc/webmaxcE.htm) while 10 mM $CaCl_2$ was added to the other. The patch pipettes were made of thin-wall borosilicate glass capillaries (1.5 OD x 1.17 ID; Harvard glass capillaries GC150T-10, Harvard Apparatus, UK). The inner wall of the glass capillaries was coated with Sigmacote (Sigma Aldrich, St. Louis, Missouri, USA) before the capillaries were drawn with a two-stage puller (PC-10, Narishige Group, Tokyo, Japan). Using a microforge (L/MCPZ 101, List Medical-Elektronic, Darmstadt, Germany), the pulled glass pipettes were coated near the tip with Sylgard (184 Silicone elastomer Kit, Dow Corning Corporation, Midland, MI, USA) and then the tips were fire-polished. Current recordings were performed at a sampling rate of 150 µs and a filter frequency at 3 kHz using an EPC800 patch clamp amplifier (HEKA Electronic). Data acquisition was carried out with the software program Pulse (HEKA Electronic). For the patch clamp experiments individual vacuoles with a membrane capacitance of 31-69 pF were used to study the channel variants under different luminal Ca^{2+} conditions. According to the voltage convention for endomembranes (*21*), the membrane potential is given for the cytosolic side of the vacuole membrane while the membrane potential at the luminal side is set to zero. The currents were measured in response to voltage pulses (1 s) in the range of -80 mV to +110 mV applied in 10 mV increments from a holding voltage of -60 mV. The steady-state current amplitudes (I_{ss}) were determined at the end of the voltage pulses and normalized to the compensated membrane capacitance (C_m) of the investigated vacuole, which was used as a measure for the vacuole membrane surface.

For conductance/voltage curves ($G/G_{max}(V)$) instantaneous tail currents (I_t) were determined from tail currents which were recorded at -60 mV after the vacuole membrane was clamped to voltage pre-pulses (1 s) in the range of -80 mV to +110 mV. Following a linear kinetic three-state model for the plant TPC1 channel ($C_2 \leftrightharpoons C_1 \leftrightharpoons O$, with two closed states $C_{1/2}$ and one open state O (*22*)), the tail currents I_t were plotted against the respective prepulse voltages and fitted with a double Boltzmann equation as follows:

$$I_t(V) = I_{max} \cdot \frac{1}{1 + \exp\left(-z_1 \cdot \frac{V-V_1}{k_B \cdot T}\right) \cdot \left(1 + \exp\left(-z_2 \cdot \frac{V-V_2}{k_B \cdot T}\right)\right)}$$

with $k_B \bullet T$ = 25.26 mV at room temperature. V_1 and V_2 give the half-activation voltages for the $C_1 \leftrightharpoons O$ and the $C_2 \leftrightharpoons C_1$ transitions, respectively. z_1 and z_2 represent the equivalent gating charges of these transitions.

The tail currents and the fits were then normalized to the maximal predicted currents (I_{max}) of the best Boltzmann fit to obtain the normalized conductance-voltage curves ($G/G_{max}(V) = I_t/I_{max}(V)$). Data were analyzed with the software programs pulse (HEKA Electronic) and Igor Pro 6.11 (Wavemetrics Inc., Lake Oswego, USA).

Statistical analysis

Data are presented as means ± SE. Significant differences $V_{1/2}$ values under 0 mM luminal Ca^{2+} conditions were analyzed with one-way-ANOVA followed by the Tukey's posthoc comparison test. To enable the statistical analysis (one-way-ANOVA with Tukey's posthoc comparison test) of the Ca^{2+}-induced shift in the $V_{1/2}$ values, the

means of the V_1 and V_2 values determined in the absence of luminal Ca^{2+} were subtracted from the individual V_1 and V_2 values, respectively, derived under 10 mM luminal Ca^{2+} conditions. Levene test and Shapiro-Wilk test confirmed assumed equal variance and normality of the data points. Sample size was not predetermined; under consideration of technical feasibility we conducted a minimum of independent patch clamp experiments on individual vacuoles per each channel construct and luminal Ca^{2+} condition. Statistical analysis was carried out with Origin 2020 (OriginLab, Northampton, Massachusetts, USA).

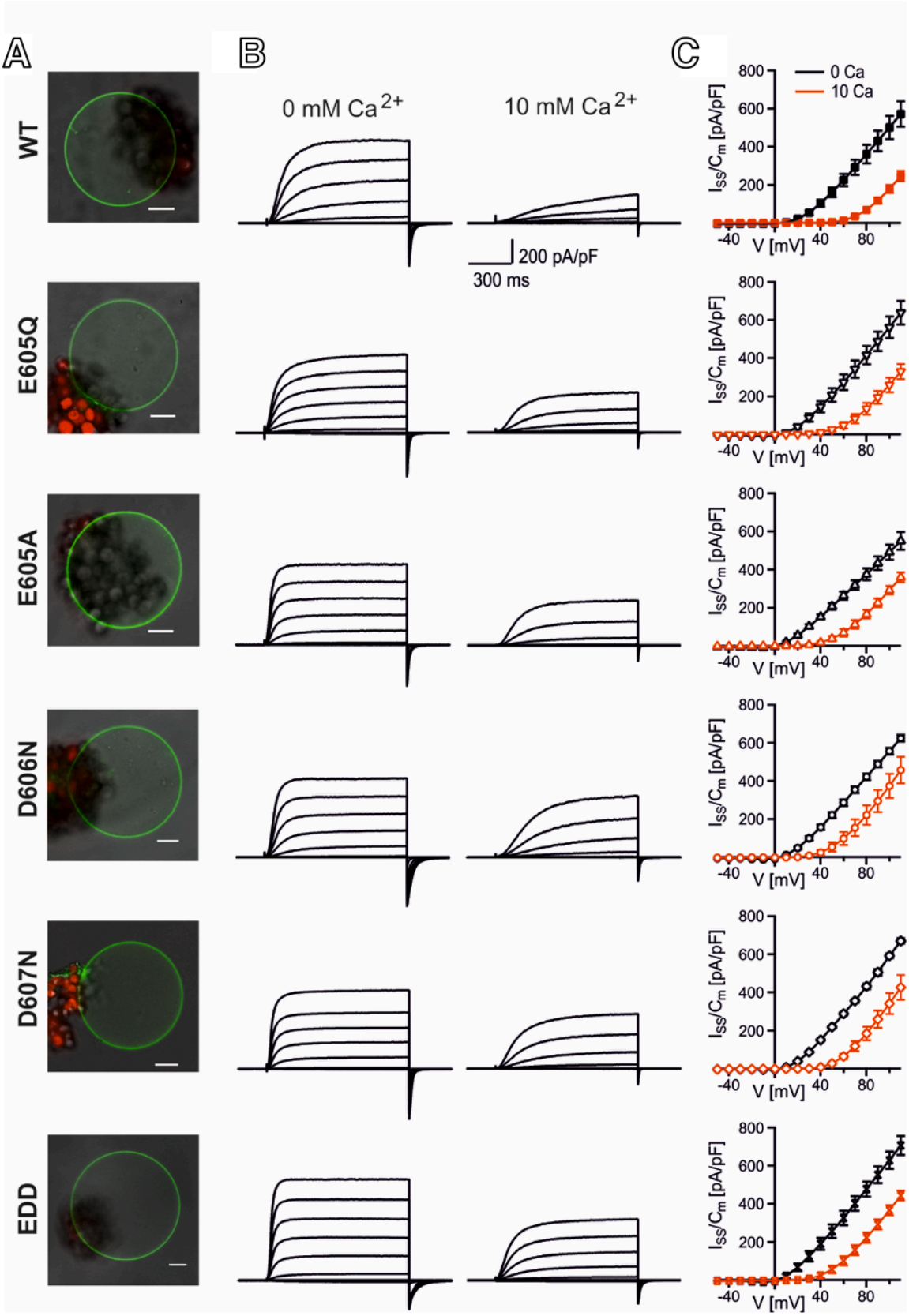
A
B
C
WT
E605Q
E605A
D606N
D607N
EDD
0 mM Ca 2+
10 mM Ca 2+
200 pA/pF
300 ms
0 Ca
10 Ca
I_SS/C_m [pA/pF]
V [mV]
800
600
400
200
-40
40
80

Figure S2.1. Electrophysiological characterization of TPC1 channel variants under different luminal Ca^{2+} conditions.
(A) Confocal images of vacuoles released from mesophyll protoplasts of the Arabidopsis mutant *tpc1-2* transiently transformed with different TPC1 channel variants which were fused to the green fluorescent protein (GFP). For all channel variants the green fluorescence signal was restricted to the vacuole membrane. Fluorescent images and bright field images were merged. Scale bar = 10 µm. **(B)** Macroscopic current responses of individual vacuoles to 1-s-lasting voltage pulses applied in the range of -80 to +110 mV in 20 mV increments in the presence (10 mM) and absence of luminal Ca^{2+}. Currents were normalized to the membrane capacitance (C_m) of the respective vacuole. The holding voltage was -60 mV. **(C)** Normalized steady-state currents (I_{ss}/C_m) plotted against the clamped membrane voltages (V) in the presence (red symbols and lines, 10 mM) and absence (black symbols and lines) of luminal Ca^{2+}. Symbols represent means ± SE. Number of experiments for each channel variant for both Ca^{2+} conditions is the same as in Figure 4. The channel variants used for the current recordings in (**B-C**) are specified in (**A**) in the same line. EDD represents the triple mutant E605Q/D606N/D607N.

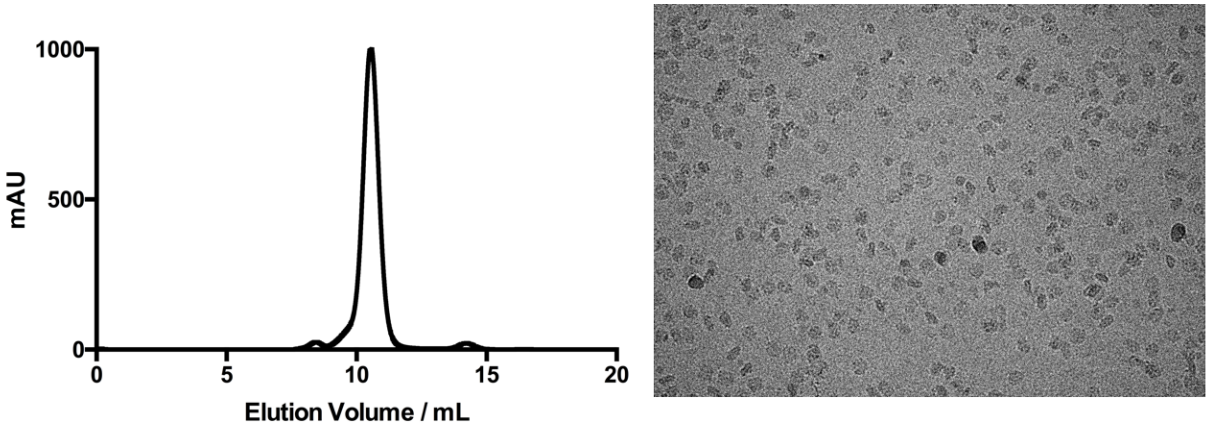

Figure S2.2. Size exclusion chromatogram (Superdex 200 increase 10/300) of GDN-solubilized AtTPC1 (left) and energy-filtered micrograph of vitreous ice-embedded particles (right).

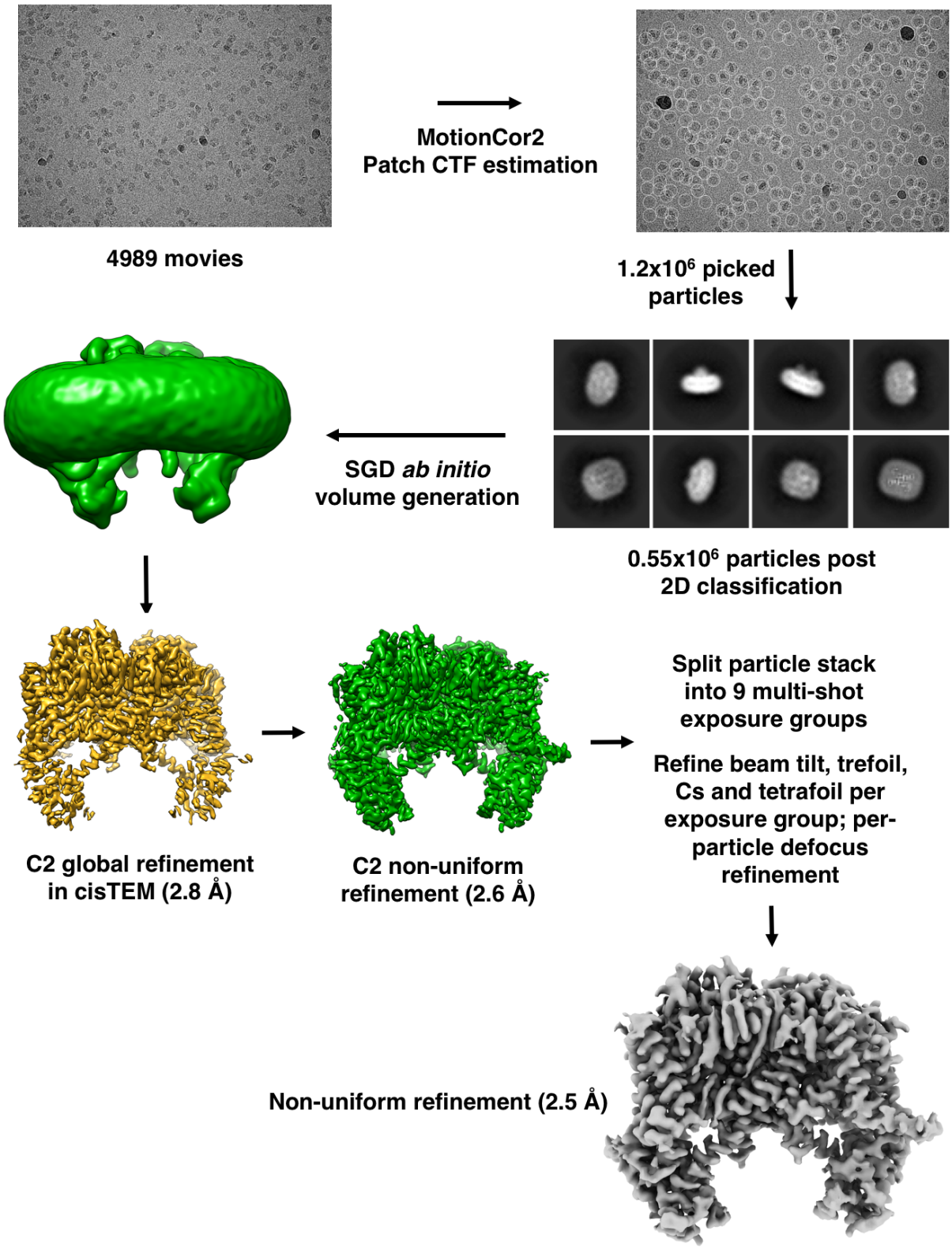

Figure S2.3) Image processing workflow for the D454N Ca^{2+} dataset.

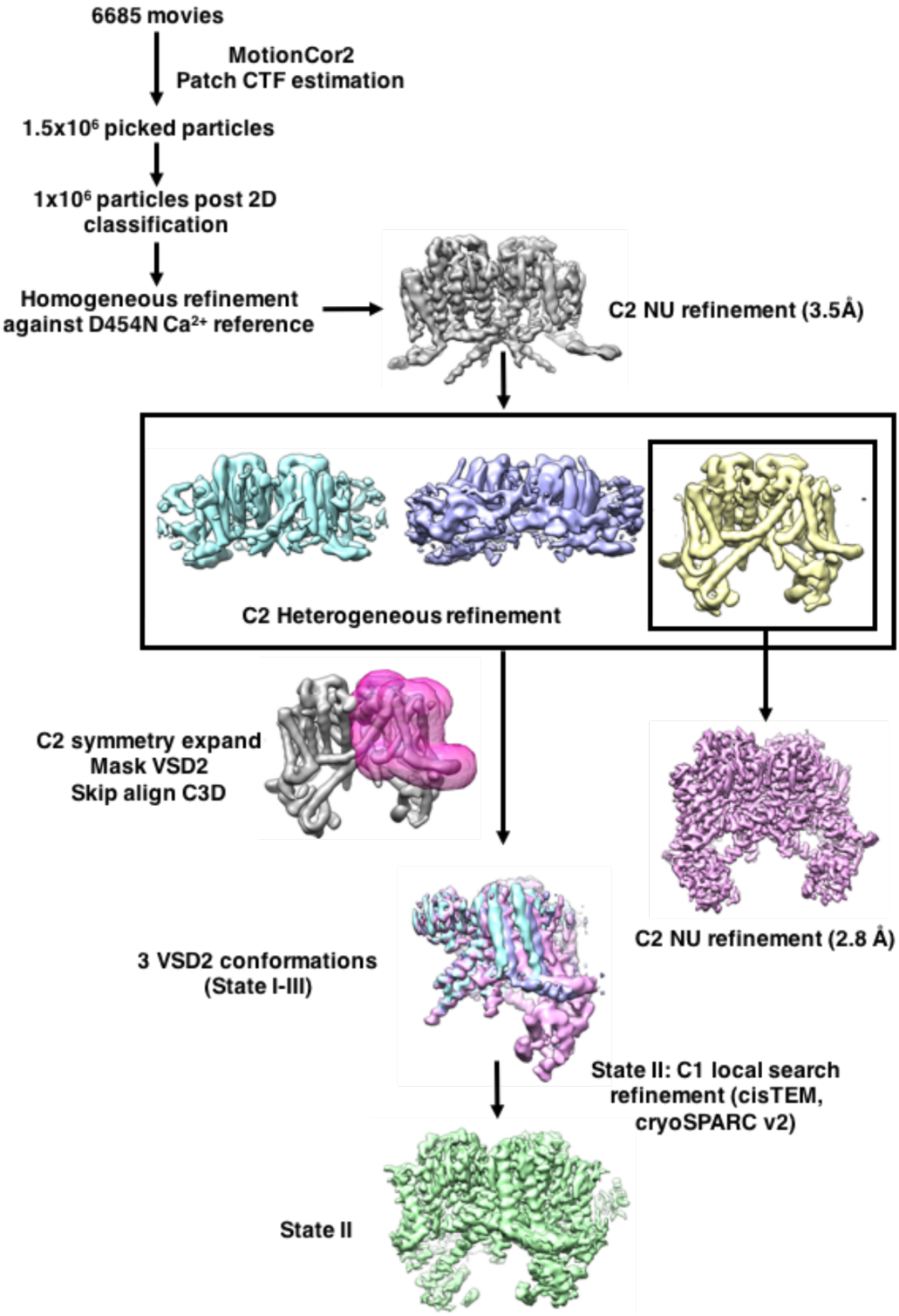
6685 movies
MotionCor2
Patch CTF estimation
1.5x10⁶ picked particles
1x10⁶ particles post 2D classification
Homogeneous refinement against D454N Ca²⁺ reference
C2 NU refinement (3.5Å)
C2 Heterogeneous refinement
C2 symmetry expand
Mask VSD2
Skip align C3D
C2 NU refinement (2.8 Å)
3 VSD2 conformations (State I-III)
State II: C1 local search refinement (cisTEM, cryoSPARC v2)
State II

Figure S2.4) Image processing workflow for the D454N EDTA dataset.

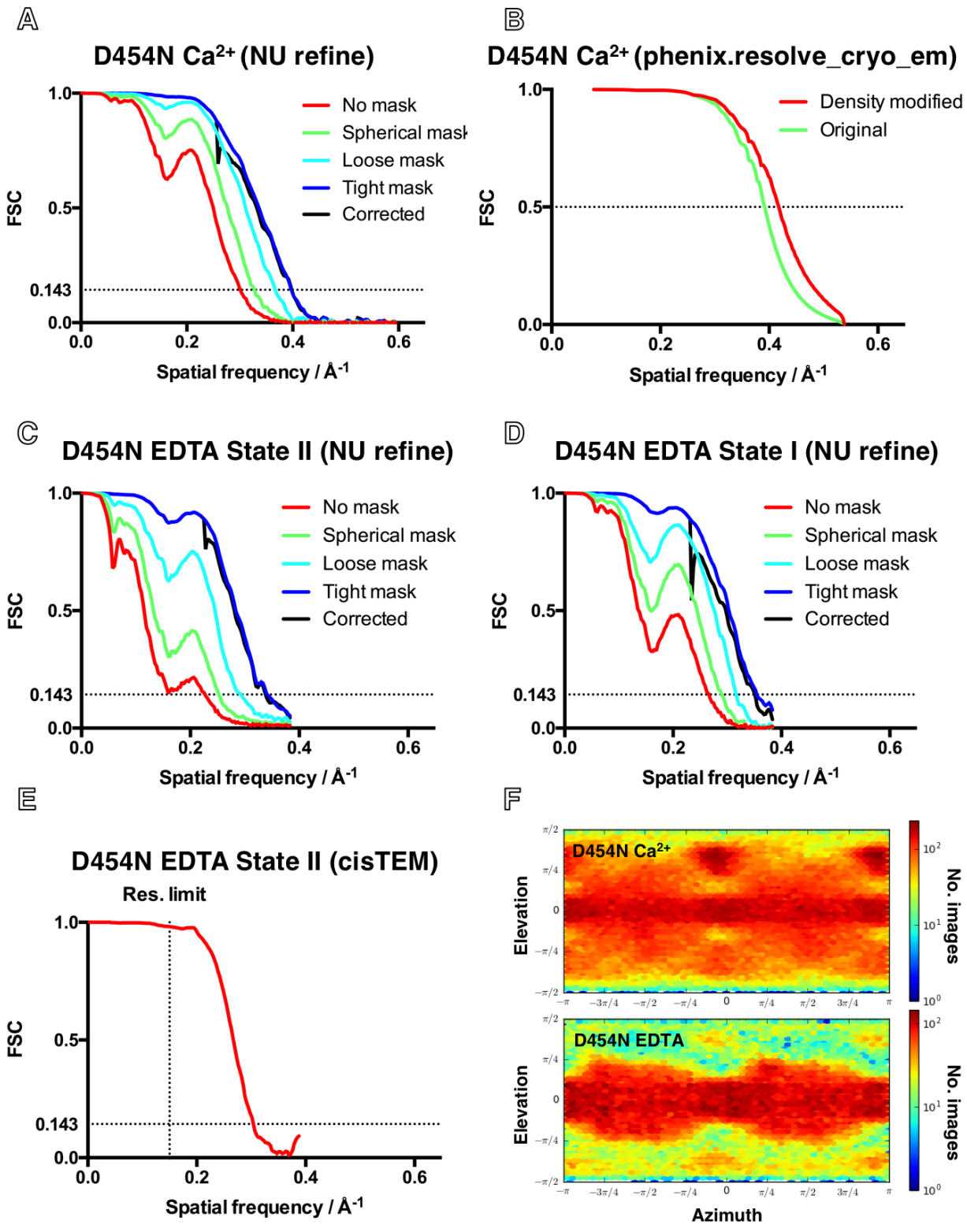

Figure S2.5) (A-E) Fourier shell correlation (FSC) resolution assessments of the various reconstructions. The cryoSPARC plots show gold standard estimations while the cisTEM plot shows solvent-corrected Part_FSC, all using a 0.143 threshold. **(F)** Euler angle plots from cryoSPARC. The **z** axis is coincident and roughly coincident with the cyclic symmetry axis for C2 and C1 reconstructions, respectively.

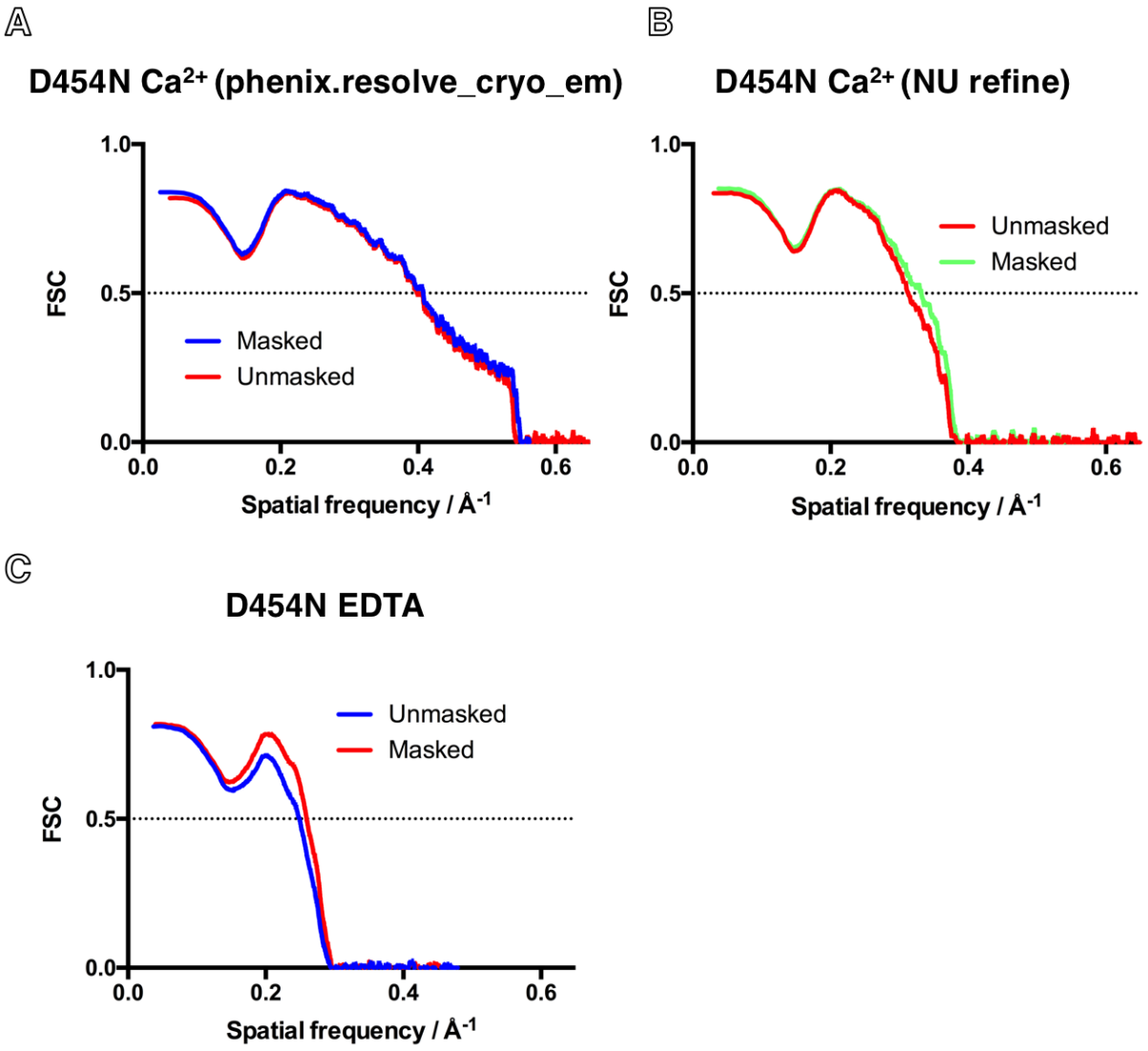

Figure S2.6) (A-C) Map to model FSC plots using a 0.5 threshold.

Supplemental Tables

Table S2.1) Ca^{2+}-induced changes in half-activation voltage V_2 for all TPC1 channel variants.

Channel variant	**V_2(10Ca)-V_2(0Ca) [mV]**	
	mean	**SE**
WT	61.0	4.2
E605Q	43.6	11.2
E605A	42.3	7.6
D606N	45.6	7.5
D607N	41.7	6.9
EDD	34.3	4.9

EDD = E605Q/D606N/D607N, SE = standard error

Table S2.2) Primers used for AtTPC1 site-directed mutagenesis.

Primer name	**Primer sequence (5'- 3')**
AtTPC1 user fwd	GGCTTAAUATGGAAGACCCGTTGATTGG
AtTPC1 user rev	GGTTTAAUTCATGTGTCAGAAGTGGAACACTC
AtTPC1 E605Q fwd	ACAGGATGACUACCTTTTGTTCAACTTCAATGAC
AtTPC1 E605Q rev	AGTCATCCTGUGCCAATTCGGTTTCAAAGAG
AtTPC1 E605A fwd	ATTGGCTGCGGAUGACTACCTTTTGTTCAAC
AtTPC1 E605A rev	ATCCGCAGCCAAUTCGGTTTCAAA
AtTPC1 D606N fwd	AGAGAATGACUACCTTTTGTTCAACTTCAAT
AtTPC1 D606N rev	AGTCATTCTCUGCCAATTCGGTTTCAAAGAG
AtTPC1 D607N fwd	AGAGGATAATUACCTTTTGTTCAACTTCAATGAC
AtTPC1 D607N rev	AATTATCCTCUGCCAATTCGGTTTCAAAGAG
AtTPC1 EDD fwd	ACAGAACAATUACCTTTTGTTCAACTTCAATGAC
AtTPC1 EDD rev	AATTGTTCTGUGCCAATTCGGTTTCAAAGAG

fwd = forward primer, rev = reversed primer

Table S2.3) Model statistics for D454N Ca^{2+} using the map obtained from phenix.resolve_cryo_em.

D454N Ca^{2+} (phenix.resolve_cryo_em)		
Composition (#)		
Chains	6	
Atoms	10112 (Hydrogens: 0)	
Residues	Protein: 1228	
Water	17	
Ligands	NA: 1	
	CA: 4	
Bonds (RMSD)		
Length (Å) (# > 4σ)	0.006 (0)	
Angles (°) (# > 4σ)	0.831 (6)	
MolProbity score	2.65	
Clash score	8.62	
Ramachandran plot (%)		
Outliers	0.17	
Allowed	5.63	
Favored	94.21	
Rama-Z (Ramachandran plot Z-score, RMSD)		
whole (N = 1208)	2.30 (0.22)	
helix (N = 890)	1.26 (0.15)	
sheet (N = 0)	--- (---)	
loop (N = 318)	1.80 (0.34)	
Rotamer outliers (%)	10.97	
Cβ outliers (%)	0.00	
Peptide plane (%)		
Cis proline/general	6.2/0.0	
Twisted proline/general	0.0/0.0	
CaBLAM outliers (%)	2.36	
Resolution Estimates (Å)	Masked	Unmasked
FSC map-model (0/0.143/0.5)	1.8/1.8/2.4	1.8/1.9/2.5

Table S2.4) Model statistics for D454N Ca^{2+} using the unmodified reconstruction.

D454N Ca^{2+}		
Composition (#)		
Chains	6	
Atoms	10271 (Hydrogens: 0)	
Residues	Protein: 1248	
Water	20	
Ligands	NA: 1	
	CA: 4	
Bonds (RMSD)		
Length (Å) (# > 4σ)	0.006 (0)	
Angles (°) (# > 4σ)	0.789 (6)	
MolProbity score	2.71	
Clash score	7.76	
Ramachandran plot (%)		
Outliers	0.16	
Allowed	5.86	
Favored	93.97	
Rama-Z (Ramachandran plot Z-score, RMSD)		
whole (N = 1228)	2.45 (0.22)	
helix (N = 862)	1.12 (0.16)	
sheet (N = 0)	--- (---)	
loop (N = 366)	2.56 (0.30)	
Rotamer outliers (%)	14.44	
Cβ outliers (%)	0.00	
Peptide plane (%)		
Cis proline/general	5.9/0.0	
Twisted proline/general	0.0/0.2	
CaBLAM outliers (%)	2.32	
Resolution Estimates (Å)	Masked	Unmasked
FSC map-model (0/0.143/0.5)	2.6/2.7/3.0	2.6/2.7/3.2

Table S2.5) Model statistics for D454N EDTA.

D454N EDTA		
Composition (#)		
Chains	2	
Atoms	10094 (Hydrogens: 0)	
Residues	Protein: 1222	
Water	0	
Ligands	0	
Bonds (RMSD)		
Length (Å) (# > 4σ)	0.010 (0)	
Angles (°) (# > 4σ)	0.917 (5)	
MolProbity score	2.26	
Clash score	15.61	
Ramachandran plot (%)		
Outliers	0.17	
Allowed	10.52	
Favored	89.32	
Rama-Z (Ramachandran plot Z-score, RMSD)		
whole (N = 1198)	3.13 (0.21)	
helix (N = 80)	3.01 (0.35)	
sheet (N = 0)	--- (---)	
loop (N = 1118)	2.27 (0.17)	
Rotamer outliers (%)	0.09	
Cβ outliers (%)	0.00	
Peptide plane (%)		
Cis proline/general	6.2/0.0	
Twisted proline/general	0.0/0.1	
CaBLAM outliers (%)	3.66	
Resolution Estimates (Å)	Masked	Unmasked
FSC map-model (0/0.143/0.5)	3.4/3.5/3.9	3.4/3.6/4.0

REFERENCES

1. M. Li *et al.*, Selecting optimum eukaryotic integral membrane proteins for structure determination by rapid expression and solubilization screening. *J. Mol. Biol.* **385**, 820–830 (2009).
2. M. Schorb, I. Haberbosch, W. J. H. Hagen, Y. Schwab, D. N. Mastronarde, Software tools for automated transmission electron microscopy. *Nat. Methods*. **16**, 471–477 (2019).
3. S. Q. Zheng *et al.*, MotionCor2: anisotropic correction of beam-induced motion for improved cryo-electron microscopy. *Nat. Methods*. **14**, 331–332 (2017).
4. T. Grant, A. Rohou, N. Grigorieff, cisTEM, user-friendly software for single-particle image processing. *Elife*. **7**, e35383 (2018).
5. J. Zivanov *et al.*, New tools for automated high-resolution cryo-EM structure determination in RELION-3. *Elife*. **7** (2018), doi:10.7554/eLife.42166.
6. A. Punjani, J. L. Rubinstein, D. J. Fleet, M. A. Brubaker, cryoSPARC: algorithms for rapid unsupervised cryo-EM structure determination. *Nat. Methods*. **14**, 290–296 (2017).
7. D. Liebschner *et al.*, Macromolecular structure determination using X-rays, neutrons and electrons: recent developments in Phenix. *Acta Crystallogr. D Struct. Biol.* **75**, 861–877 (2019).
8. A. F. Kintzer, R. M. Stroud, Structure, inhibition and regulation of two-pore channel TPC1 from Arabidopsis thaliana. *Nature*. **531**, 258–262 (2016).
9. J. Guo *et al.*, Structure of the voltage-gated two-pore channel TPC1 from Arabidopsis thaliana. *Nature*. **531**, 196–201 (2016).

10. P. Emsley, B. Lohkamp, W. G. Scott, K. Cowtan, Features and development of Coot. *Acta Crystallogr. Sect. D, Biol. Crystallogr.* **66**, 486–501 (2010).
11. R. T. Kidmose *et al.*, Namdinator - automatic molecular dynamics flexible fitting of structural models into cryo-EM and crystallography experimental maps. *IUCrJ*. **6**, 526–531 (2019).
12. E. F. Pettersen *et al.*, UCSF Chimera—a visualization system for exploratory research and analysis. *J. Comput. Chem.* **25**, 1605–1612 (2004).
13. E. Peiter *et al.*, The vacuolar Ca2+-activated channel TPC1 regulates germination and stomatal movement. *Nature*. **434**, 404–408 (2005).
14. H. H. Nour-Eldin, B. G. Hansen, M. H. H. Nørholm, J. K. Jensen, B. A. Halkier, Advancing uracil-excision based cloning towards an ideal technique for cloning PCR fragments. *Nucleic Acids Res.* **34**, e122 (2006).
15. G. Zhang, V. Gurtu, S. R. Kain, An enhanced green fluorescent protein allows sensitive detection of gene transfer in mammalian cells. *Biochem. Biophys. Res. Commun.* **227**, 707–711 (1996).
16. B. Dadacz-Narloch *et al.*, A novel calcium binding site in the slow vacuolar cation channel TPC1 senses luminal calcium levels. *Plant Cell*. **23**, 2696–2707 (2011).
17. T. Asai *et al.*, MAP kinase signalling cascade in Arabidopsis innate immunity. *Nature*. **415**, 977–983 (2002).
18. S.-D. Yoo, Y.-H. Cho, J. Sheen, Arabidopsis mesophyll protoplasts: a versatile cell system for transient gene expression analysis. *Nat. Protoc.* **2**, 1565–1572 (2007).
19. B. Dadacz-Narloch *et al.*, On the cellular site of two-pore channel TPC1 action in the Poaceae. *New Phytol.* **200**, 663–674 (2013).

20. L. Lagostena, M. Festa, M. Pusch, A. Carpaneto, The human two-pore channel 1 is modulated by cytosolic and luminal calcium. *Sci. Rep.* **7**, 43900 (2017).

21. A. Bertl *et al.*, Electrical measurements on endomembranes. *Science*. **258**, 873–874 (1992).

22. I. I. Pottosin, M. Martínez-Estévez, O. R. Dobrovinskaya, J. Muñiz, G. Schönknecht, Mechanism of luminal Ca2+ and Mg2+ action on the vacuolar slowly activating channels. *Planta*. **219**, 1057–1070 (2004).